NONLINEAR VIBRATION OF ROTOR-BEARING SYSTEM WITH SQUEEZE FILM DAMPING

A THESIS SUBMITTED TO
THE GRADUATE SCHOOL OF NATURAL AND APPLIED SCIENCES
OF
MIDDLE EAST TECHNICAL UNIVERSITY

BY

FURKAN SEVENCAN

IN PARTIAL FULFILLMENT OF THE REQUIREMENTS
FOR
THE DEGREE OF MASTER OF SCIENCE
IN
MECHANICAL ENGINEERING

AUGUST 2022

Approval of the thesis:

NONLINEAR VIBRATION OF ROTOR-BEARING SYSTEM WITH SQUEEZE FILM DAMPING

submitted by **FURKAN SEVENCAN** in partial fulfillment of the requirements for the degree of **Master of Science** i**n Mechanical Engineering, Middle East Technical University** by,

Prof. Dr. Halil Kalıpçılar
Dean, Graduate School of **Natural and Applied Sciences** _____

Prof. Dr. Sahir Arıkan
Head of the Department, **Mechanical Engineering** _____

Prof. Dr. Ender Ciğeroğlu
Supervisor, **Mechanical Engineering, METU** _____

Assist. Prof. Dr. Özgür Uğraş Baran
Co-Supervisor, **Mechanical Engineering, METU** _____

Examining Committee Members:

Assist.Prof. Dr. Gökhan Özgen
Mechanical Engineering, METU _____

Prof. Dr. Ender Ciğeroğlu
Mechanical Engineering, METU _____

Assist. Prof. Dr. Özgür Uğraş Baran
Mechanical Engineering, METU _____

Assist. Prof. Dr. Orkun Özşahin
Mechanical Engineering, METU _____

Assist. Prof. Dr. Mohammad Rahmanian
Aeronautical Engineering, Gebze Technical University _____

Date: 31.08.2022

I hereby declare that all information in this document has been obtained and presented in accordance with academic rules and ethical conduct. I also declare that, as required by these rules and conduct, I have fully cited and referenced all material and results that are not original to this work.

Name Surname : Furkan Sevencan

Signature :

ABSTRACT

NONLINEAR VIBRATION OF ROTOR-BEARING SYSTEM WITH SQUEEZE FILM DAMPING

Sevencan, Furkan
Master of Science, Mechanical Engineering
Supervisor: Prof. Dr. Ender Ciğeroğlu
Co-Supervisor: Assist. Prof. Dr. Özgür Uğraş Baran

August 2022, 70 pages

Squeeze film damper is a widely used nonlinear element in rotor-bearing systems. The dynamic behavior of the rotor-bearing system supported by the squeeze film damper must be investigated for proper design and analysis. Nonlinear vibration response of rotor systems supported by squeeze film damper due to unbalance is investigated. The system rotordynamic model is developed using 1D Timoshenko beam elements. Three types of modeling are performed for SFD. The nonlinear SFD models are based on the analytical solution of the Reynolds equation for open ends short length SFDs and the numerical solution of the 3D Reynolds equation of flow model by using the Finite Difference Method (FDM) for open ends SFDs by considering oil inertia effects. As FDM is computationally cost, a neural network study is performed for various parameters related to SFD. Finally, Neural Network simulation is performed using data set obtained from the 3D Reynolds equation of flow model using the Finite Difference Method (FDM) for open ends SFDs. Rotor-bearing system and SFD are incorporated, and a nonlinear equation of motion is obtained. Harmonic Balance Method (HBM) takes place to represent the resulting

nonlinear differential equations of motion as a set of nonlinear algebraic equations. Newton Method with arc-length continuation is utilized as the solution method for the set of nonlinear algebraic equations obtained. Case studies are performed to investigate the effects of SFD parameters and compare SFD modeling approaches in accuracy and computational time.

Keywords: Rotordynamic, Squeeze Film Damper, Nonlinear Vibrations

ÖZ

SIKIŞAN FİLM SÖNÜMÜ BARINDIRAN ROTOR-RULMAN SİSTEMLERİN DOĞRUSAL OLMAYAN TİTREŞİMİ

Sevencan, Furkan
Yüksek Lisans, Makina Mühendisliği
Tez Yöneticisi: Prof. Dr. Ender Ciğeroğlu
Ortak Tez Yöneticisi: Dr. Öğr. Üyesi Özgür Uğraş Baran

Ağustos 2022, 70 sayfa

Sıkışan film sönümü , rotor-yatak sistemlerinde yaygın olarak kullanılan doğrusal olmayan bir elemandır ve sıkışan film sönümü barındıran rotor-yatak sistemlerinin dinamik davranışı uygun tasarım ve analizler için dikkatlice incelenmelidir. Sıkışan film sönümü ile desteklenen dönen sistemlerinin balanssızlıktan kaynaklanan doğrusal olmayan titreşim tepkisi incelenmiştir. Sistemin rotor dinamik modeli, 1 boyutlu Timoshenko kiriş elemanları kullanılarak geliştirilmiştir. SFD için üç tip modelleme yapılır. Doğrusal olmayan SFD modelleri, sızdırmazlık elemanı barındırmayan kısa uzunluklu SFD için Reynolds denkleminin analitik çözümüyle ve sızdırmazlık elemanı barındırmayan SFD için yağın kütle etkisi de dahil edilerek Sonlu Fark Metodu (FDM) kullanılarak 3 boyutlu Reynolds akış denkleminin sayısal çözümüyle elde edilmiştir. FDM kullanılan çözüm yavaş olduğu için SFD ile ilgili çeşitli parametreler için bir sinir ağı çalışması yapılmıştır. Son olarak, açık uçlu SFD için Sonlu Fark Metodu (FDM) kullanılarak akış modelinin 3B Reynolds denkleminden elde edilen veri seti kullanılarak Sinir Ağı simülasyonu gerçekleştirilmiştir. Rotor-yatak sistemi modeli ve SFD modeli bir araya getirilerek doğrusal olmayan hareket denklemi elde edilmiştir. Harmonik Denge Yöntemi (HBM), elde edilen doğrusal olmayan diferansiyel hareket denklemlerini bir dizi

doğrusal olmayan cebirsel denklem olarak temsil etmek için kullanılmıştır. Elde edilen doğrusal olmayan denklemler için çözüm yöntemi olarak yay uzunluğu sürdürme yöntemi ile Newton Metodu kullanılmıştır. SFD parametrelerinin etkilerini araştırmak ve SFD modelleme yaklaşımlarını doğruluk ve hesaplama süresi açısından karşılaştırmak için çeşitli analiz çalışmaları gerçekleştirilmiştir.

Anahtar Kelimeler: Rotordinamiği , Sıkışan Film Sönümü , Doğrusal Olmayan Titreşim

To My Father, in Loving Memory

and

My Family

ACKNOWLEDGMENTS

I would like to express my gratitude to my supervisor Prof. Dr. Ender Ciğeroğlu, for his unique guidance, support, and patience. I would also like to thank my co-supervisor, Assist. Prof. Dr. Özgür Uğraş Baran for his contributions.

I'm grateful to my family, who supported and encouraged me, as they always have done throughout my life.

I would like to express my appreciation to Dr. Emre Dikmen, who introduced me to the field of rotor dynamic, for his endless support and guidance. I would also like to thank Mr. Reşit Kayhan Ata for their technical support.

I would like to acknowledge the support provided by TRMOTOR Güç Sistemleri A.Ş gratefully.

TABLE OF CONTENTS

LIST OF TABLES

TABLES

LIST OF FIGURES

FIGURES

CHAPTER 1

INTRODUCTION

1.1 Problem Statement

The most common Rotordynamic problems are excessive steady state vibration levels and rotor instabilities [1,2]. One of the most critical solutions is introducing external damping to the system. In rotor-bearing systems, the external damping source is a Squeeze Film Damper (SFD), known as one type of journal bearing. Squeeze Film Dampers have been commonly used in rotor-bearing systems such as gas turbines, aero engines, and high-speed machinery to reduce vibration levels and assist the stability of rotor-bearing systems [3,4]. Rotordynamic evaluation is necessary to assess the dynamic behavior of rotor-bearing systems, so adequate modeling for rotordynamic behavior and SFD is essential for rotor-bearing systems, which include SFD. The force generated by SFD depends on displacement at the SFD location, which makes the system nonlinear in the aspect of mechanical vibrations. Nonlinear vibration of a rotor-bearing system supported by SFD under unbalance excitation, which is the primary source of external forcing for rotating systems, can be investigated by developing a rotordynamic model for the rotor-bearing system and flow model for squeeze film damper (SFD). Incorporating these models with a nonlinear solver is to be achieved for proper design and analysis of the rotor bearing system supported by SFD.

Analytical solutions for SFD under some fundamental assumptions and simplified rotor bearing system solutions such as rigid rotor assumption on flexible bearings are available in the literature. Although they give an idea about the effects of SFD and the dynamic behavior of the systems, their results are limited by their

fundamental assumptions. A more complex and accurate solution for the problem is desired. Although the Computational Fluid Dynamics (CFD) solution for SFD and many degrees of freedom (DOFs) models for rotor-bearing systems can be used for the problem, it is costly regarding computational time. A more computationally efficient solution is desired for the problem. In nonlinear vibration problems, the steady-state response solution in the frequency domain is faster than the time domain solution. 1D FE-based rotordynamic model is developed to model rotor-bearing system, and flow model is developed to represent squeeze film damper pressure distribution using 1D Reynolds equation and finite difference method (FDM). Steady-state nonlinear vibration of the rotor-bearing system supported by SFD is studied by assembling these rotordynamic and flow models and solved with nonlinear methods.

1.2 Literature Survey

Squeeze Film Dampers are lubricated elements commonly used in rotor-bearing systems to provide damping and structural isolation, reduce vibration levels due to unbalance excitation and increase the stability margins [5]. Squeeze film damper (SFD) consists of oil film, which creates energy dissipation, stiffness, and fluid inertia. The schematic view of the SFD is given in Figure 1.1. The annular oil film is filled between the journal on the outer bearing race and housing on the stationary components. Oil film's inner and outer race does not spin with the spin of the shaft by means of anti-rotation pin usage, which differs from squeeze film damper from journal bearing. Its working principle and usage resemble journal bearing; however, its inner race does not spin. The journal and housing have almost the same diameter; the oil film clearance is very small. Dynamic forces acting on the system lead to journal movement, then hydrodynamic squeeze film pressure is exerted due to oil film displacement.

The generated pressure distribution acts on the system as reaction forces, attenuating the transmitted force and reducing the vibration amplitudes. Therefore, SFD comes up with damping due to viscous dissipation force and mass contribution due to the fluid inertia effects. Moreover, SFD does not create direct stiffness; it may create cross-coupled damping depending on the cavitation on the oil film. The centering spring mechanism achieves desired motion capability of an oil film. In most aircraft engines, SFD is used with a flexible centering mechanism such as a squirrel cage, which provides soft support and centers the journal's motion. As the damping performance of the SFD depends on the fluid displacement of the oil film, desired centering spring element is designed and utilized. Squeeze film damper arrangement with centering spring mechanism (squirrel cage) is given in Figure 1.2 [3].

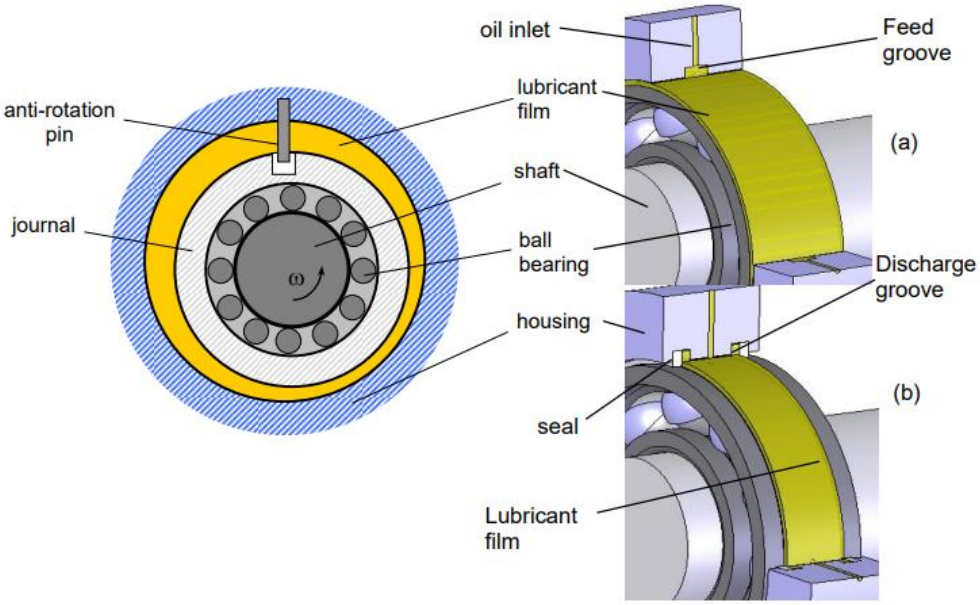

Figure 1.1: Squeeze Film Damper Configurations a) SFD with central feed groove b.) SFD with end groove and seals [5]

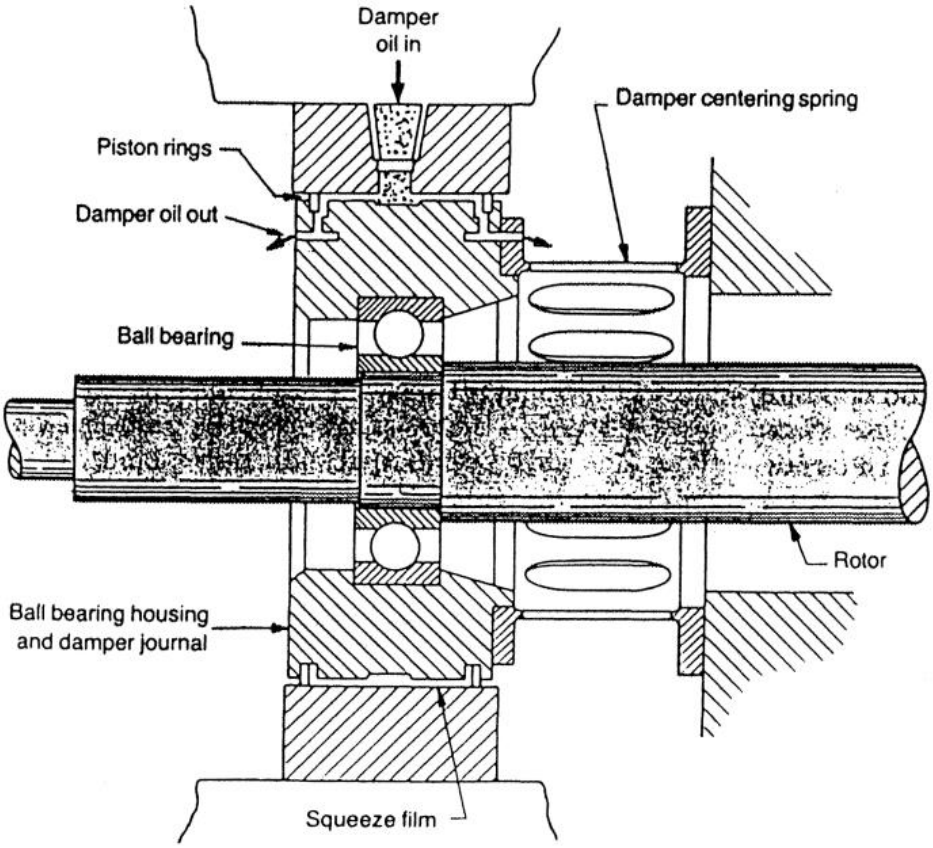

Figure 1.2: SFD arrangement with Squirrel Cage [3]

Because of the risk of instability due to fluid film bearings, journal bearings are not used in most aircraft engines. Short-length SFD is generally preferred in aircraft engines due to low weight and small space requirements in aero engines. Squeeze Film Damper's geometrical parameters, such as length of the oil film, the diameter of the damper and clearance of the oil film, and lubrication properties such as viscosity and density of used oil, are the effects of the main parameters on SFD performance. Furthermore, the type of SFD configuration, such as end seal usage, supply & discharge conditions, the effect of lubricant cavitation, and the effect of fluid inertia, are essential considerations for the performance of SFD.

Cooper conducted one of the pioneer studies about SFD [6]. He experimentally investigated SFD performance; this experimental study's result shows why it is used

in most turboshaft and turbojet engines. Three different bearing configuration is compared in the study at low speeds. He observed small-sized, intermediate-sized, and large-sized orbits, and White [7] continued the investigation. White reveals that the intermediate-sized orbit is unstable, so the motion jumps from one to another. The jump phenomenon is observed due to the nonlinearity of squeeze film force. One of the most critical quantitative results of White's study is that radial clearance of the damper shall be at least 2.3 times larger than the imbalance eccentricity exerted on the damper to keep the small-sized inverted orbit motion.

Zeidan et al. [8] provide good insight to the researchers about SFD design and its application in jet engines. They mentioned the nonlinearity of SFD and the jump phenomenon and summarized the effects of end seal usage, feeding oil into oil film, fluid inertia, and cavitation effects. Arauz and San Andres [9] conducted an experimental study for SFD with a circumferential feed groove. The study shows that feeding grooves contribute to Squeeze Film Damper's damping capability. Arauz and San Andres [10] compared piston ring sealed SFD and open-end SFD configurations and presented the measurements for forces generated by SFDs. They found that even if sealed SFD oil's temperature increased, the damping capacity of sealed SFD is higher than open-ended SFD configuration. San Andres and Vance [11] have studied the effects of fluid inertia on the performance of SFD. The study shows that fluid inertia effects on the SFD performance cannot be disregarded under certain operating conditions. Reynolds number is the most influential parameter on the relevance of the fluid inertia of the lubricant. Cavitation on the oil film may be occurred due to insufficient external pressurization or/and excessive leakage on the end seals. Cavitation effects and their theoretical modeling has been studied by plenty of researchers. The experimental study was conducted by Zeidan [12], and it is observed that two types of cavitation (vapor and gaseous). The results reveal that gaseous cavitation highly diminishes the damping capability of the oil film region in SFD, and cavitation distribution is more than half of a circle.

The performance of Squeeze Film Damper is mainly related to damper design parameters, operating conditions of the damper, and acting unbalance loading on the

damper, so SFD effects on rotordynamic behavior of rotor-bearing systems have been studied for a long time. Force coefficients of SFD can be obtained by solving related Navier Stokes Equation or Reynold equation analytically. The second solution method is limited by some assumptions. Gunter [3] came up with force coefficients with the circular center orbit (CCO) assumed motion for the central groove with an open end. San Andres and Vance [13] show force coefficients with off-centered orbit motion types for open-ended and long-bearing assumptions, including fluid inertia effects. Moreover, approximated coefficients for finite-length bearing are concluded by employing correlation factors on long damper formulations. The theoretical force coefficients of SFD, stiffness, and damping coefficients are summarized by Vance [1] for open-ended SFD under the assumptions of short/long bearing and cavitated / uncavitated. San Andres [14] conducted an experimental study to compare the theoretical formulation of short-length assumed force coefficients. Fluid film forces are measured experimentally for fully submerged open-end squeeze film dampers with rotor speed up to 5000 cpm and low pressures. The experimental study, such as journal orbit motion, is 30-50 percent of damper clearance. The results show a good correlation for fully submerged open-end SFD up to whirl frequency to 524 rad/s and low supply pressure. It is also observed that the formulation for half film cavitation agrees well with the experiments at higher whirl frequencies and no oil cavitation agrees well with the experiments at lower whirl frequencies.

The incorporation of SFD in rotordynamic systems is investigated for different rotordynamic models, such as rigid rotor assumption, simple, flexible rotors, and complex multi-mass flexible rotors. In the rigid rotor modeling approach, the support is highly flexible with respect to the shaft, so the shaft's flexibility is not considered. Taylor et al. [15,16] investigated steady–state dynamic behavior of rigid rotors on Squeeze Film dampers. Mohan and Hahn [17] studied theoretically on a rigid rotor supported by a short SFD, and the π-film cavitation model was assumed as the cavitation type. The motion type of the SFD journal is taken as CCO, and the effect of SFD parameters and unbalance loadings on the response is investigated. Hahn

[18] modeled SFD using short bearing assumption and Warner approximation to determine the critical unbalance for the rigid rotor. Cookson and Kossa [19] studied the off-centered rigid rotor's transient response and different SFD parameters. SFD with centering spring and without centering spring effects on steady-state response are investigated. The rotor's mass is lumped at the middle of the rotor, or the mass is shared by bearing centers and rotor center. These kinds of rotors are called simple, flexible rotors, such as Jeffcott Rotors. Rabinowitz and Hahn [20,21] conducted a theoretical study on the steady-state response of a simple, flexible rotor supported by unpressurized short-length SFD, which carries out CCO motion, and Routh-Hurwitz criteria are used to analyze the stability of the system. Zhou [22,23] shows that under high unbalance loading SFD supported flexible rotor may experience bistable jump and chaotic motion. Inayat-Hussain et al. [24,25] performed a bifurcation analysis of a simple, flexible rotor with SFD and the effects of SFD design parameters and operational conditions on the margin speed for bifurcation. FE-based rotordynamic models give more accurate results than rigid rotor or simple, flexible rotor modeling. Modeling the multi-mass rotor-bearing system is essential for investigating the dynamic behavior of rotating systems. Nelson studied a multi-degree of freedom rotor-bearing system model using the Timoshenko beam element [26]. Genta [27] worked on advanced rotordynamic finite element modeling, including gyroscopic effects and reduction techniques. Multi-mass flexible rotors incorporated with SFD are studied in the literature. Nelson [28] studied an iterative solver for a flexible rotor-bearing system supported by a Squeeze film damper. The modified secant root finding method is developed to solve damper eccentricity and obtain force coefficients for every operating speed. McLean and Hahn [29] studied the forced response of flexible rotor-bearing systems supported by SFDs due to unbalance excitation. The solution method for nonlinear equations is significant in the aspect of computational time. Bonello [30] suggested the usage of an improved receptance harmonic balance method (RHBM) to the solution of the nonlinear vibration problem.

The studies mainly focus on the modeling approach for SFD as analytical solutions of the related fluid equation under some assumptions and ignore the inertia effects of the oil film. Another modeling approach for SFD is the Finite Difference Method (FDM) which is a more complex modeling of Squeeze film dampers. The finite length of SFD, effects of end sealing, effects of feeding and discharging, and cavitation types can be included without fundamental assumptions for the numerical solution of 2D pressure distribution of SFD. Lund [31] and Tecza [32] obtained two-dimensional pressure distribution by utilizing the finite difference method (FDM) and conducted an experimental study to analyze the effects of oil holes, oil grooves, and fluid inertia on damping performance. San Andres [33] studied the effects of fluid inertia by using FDM on the synchronous response of flexible rotors supported by SFD. Results indicate that rotor amplitude and transmitted force significantly decreased while the Reynolds number increased. Hamzehlouia et al. [34-36] solved the 2D Reynolds equation with the FDM method for open-ended SFD, which executes CCO motion and considers fluid inertia effects by the first-order pressure perturbation method. Reynolds number, eccentricity ratio, and length over diameter parameters are investigated on the pressure distribution and dynamic response of multi-mass flexible rotor supported by SFD. Extensive experimental studies are conducted about different effects, such as fluid inertia, lubricant cavitation, air ingestion pressurization, and sealing, summarized by San Andres et al. [37]. Feng He et al. [38] used Harmonic Balance Method (HBM) to obtain a set of nonlinear algebraic equations from the differential equation of motion for the forced response of a 1D finite element-based rotor-bearing system supported by short length SFD including fluid inertia effects. It is observed that The HBM is computationally 5-12 times faster than traditional transient methods such as Runge-Kutta, with similar results. Responses are studied for varying unbalance loadings, the location of unbalance loadings, and varying stiffness of springs connected with the dampers. Furthermore, the predictor-corrector solution method is utilized. Chen et al. [39] analyzed the rotor-bearing system supported by SFD, which is modeled as a short-length bearing assumption without considering fluid inertia under the base

excitation. They showed the nonlinear vibration behavior for different unbalance loading conditions and investigated the viscosity of used oils. Later Chen et al. [40] presented the same system by considering fluid inertia effects on the SFD. The paper used the FDM solution for open-ended SFD and compared only viscous effects acting nonlinear response, and fluid inertia effect included nonlinear response. The results show that fluid inertia effect inclusion in Reynold oil film equation increases viscous dissipation's damping capability on vibration responses.

Harmonic Balance Method (HBM) is widely used for nonlinear algebraic equations, and the Newtons Method with arc-length continuation is utilized as a solver type for nonlinear vibration problems. Von Groll and Ewins [41] uses the indicated procedures for nonlinear vibration problems about rotor stator contact. Furthermore, Receptance Method is used to significantly reduce the nonlinear algebraic equation numbers on the MDOF systems [42,43].

1.3 Motivation and Scope

As SFD is not an on-shelf element, it should be designed for specific rotor-bearing systems. Nonlinear vibration of the rotor-bearing system supported by SFD should be investigated for proper design and analysis. In literature, it is seen that some methods are suggested to analyze the dynamics behavior of rotor-bearing systems supported by SFD. Most of them consider analytical solutions for SFD, which are available only for limited conditions such as pressure gradient is negligible either circumferentially or axially. Furthermore, oil inertia effects on vibration responses are primarily neglected in these studies, which may change responses drastically. 3D pressure distribution solution considering these effects is utilized for rotor-bearing systems supported by SFD; however, they are most probably computationally cost.

In this study, the nonlinear vibration of the rotor-bearing system supported by SFD due to unbalance excitation is investigated. An advanced rotordynamic model is established for modeling rotor-bearing systems. Firstly, SFD is modeled with an

analytical solution of the Reynolds equation, and the effects of SFD and the amount of unbalance load are investigated. Secondly, the 3D pressure distribution is solved using FDM to consider oil inertia effects and obtain no limitations for the SFD length-to-diameter ratio. Force coefficients are obtained by numerical integration of pressure distributions. Lastly, using the stated FDM solution, a neural network study is performed to model SFD for a wide range of non-dimensional parametric inputs and generated force coefficient outputs. The analysis leads to getting as accurate as FDM solution and computationally efficient with respect to FDM. Receptance Method (RM) is used to reduce rotor-bearing system DoFs and reduce nonlinear differential equations. HBM is used to obtain nonlinear algebraic equations representing steady-state vibrations, and Newton's method with arc-length continuation is used as the solution method. A small turbojet engine, given in [27], is used for the case studies. Various parametric changes are applied, and the results are compared in the aspect of accuracy and computational time.

CHAPTER 2

MATHEMATICAL MODELING

In this chapter, mathematical modeling of the rotordynamic model and SFD model are explained. Rotor-bearing system modeled using FEM with linear 1D Timoshenko beam elements, including gyroscopic effects. SFD is modeled in 3 different ways. The first is the SFD model with the analytical solution of the Reynolds Equation of short-length SFD. Secondly, SFD model with Finite Difference Method (FDM) solution of 3D Reynolds Equation of SFD. Lastly, SFD model with Neural Network simulation by utilizing FDM solution of 3D Reynolds Equation of SFD.

2.1 Rotordynamic Model with FEM

Rotordynamic is the branch of applied mechanics concerned with the behavior of dynamics of rotating systems. Natural frequency changes with the spin velocity of the rotor system due to the presence of gyroscopic effects. The modes that increase with the spin speed are called forward whirling modes, and the modes that decrease with speed are called backward whirling modes.

Finite Element Modeling (FEM) is commonly used to represent the rotor-bearing system model. FEM is implemented to model rotor-bearing components such as shafts, disks, linear bearing, and stiffness and damping of the bearing and support structure as simple mass, spring, and damper elements. Nelson and McVaugh [44] are one of the first developer FEM for rotordynamic analysis. Three dimensional (3D) linear beam elements are established by using 6-DOF (3 translational and 3 rotational) for one side of the beam node and 6- DOF for the other side of the beam

element, and Euler-Bernoulli and Timoshenko beam formulations are used for finite element model of flexible elements. In lateral vibration investigation, 1 translational DOF related to the axial direction of the rotor and 1 rotational DOF associated with the torsional direction spin direction is ignored. Therefore, 8 DOF Timoshenko beam element is utilized in rotordynamic modeling.

The rotor-bearing system, which consists of flexible shafts, disks, and bearings, is modeled based on a 1D finite element method. Timoshenko beam elements with 4 degrees of freedom (DOF) per each node for lateral directions (x, y, θ_x, θ_y) are used for the flexible shaft. The components such as compressors, turbine disks, and blades are modeled as lumped masses, including diametral and polar mass moment inertia of the members as the shaft vibration is studied. Disks are considered rigid as local disk modes are not considered in the rotor dynamic model. Bearings are represented as linear springs and viscous damping elements between the bearing connection node and the ground.

Stiffness, damping, and mass matrices are obtained for the rotor-bearing system. Additionally, gyroscopic effects must be included in rotor-bearing system modeling, so gyroscopic matrices are obtained. Entire system matrices derived and detailed information related to system matrices can be found [27]. The geometrical presentation of the beam element is given in Figure 2.1.

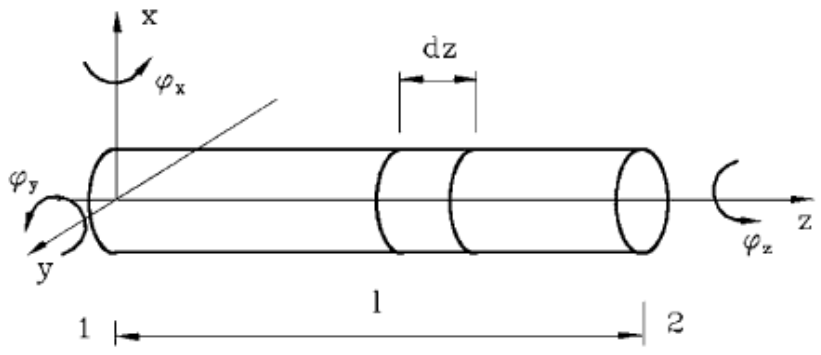

Figure 2.1: Geometrical representation of beam element [27]

2.2 Squeeze Film Damper(SFD) Model

Squeeze film damper (SFD) consists of oil film, which creates energy dissipation, stiffness, and fluid inertia. The schematic view of the SFD is given in figure #1. The oil film is filled between the journal and the housing. The journal does not spin due to the presence of an anti-rotation pin. The geometrical parameters of the SFD, such as length, diameter, and clearance, are shown in Figure 2.2.

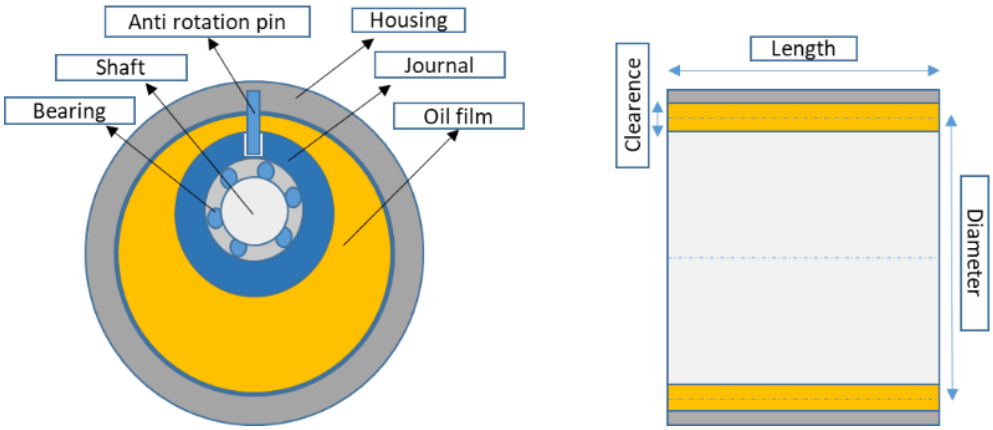

Figure 2.2: Schematic of SFD

The forces due to SFD can be obtained by solving the pressure distribution on the SFD journal surfaces by utilizing the Reynolds equation as given [5]:

$$\frac{\partial}{R\partial\theta}\left(\frac{\rho h^3}{\mu}\frac{\partial p}{R\partial\theta}\right)+\frac{\partial}{\partial z}\left(\frac{\rho h^3}{\mu}\frac{\partial p}{\partial z}\right)=12\frac{\partial(\rho h)}{\partial t} \tag{2-1}$$

Where h is the dynamic film thickness p, μ and ρ are the pressure of the oil film, viscosity, and density of the oil, respectively. θ is the circumferential direction in cylindrical coordinates and z is the axial direction of the SFD. The dynamic film thickness h, can be defined as:

$$h = c + e\cos(\theta) \tag{2-2}$$

c is the radial clearance of the SFD and e is the dynamic amplitude of the SFD.

The Reynolds equation can be solved in two ways. The first is the analytical solution, which requires simplifying the equation and solving pressure distribution in 1D. The second is the finite difference method (FDM) solution which solves the pressure distribution of the field in 2D. The model of SFD can be solved in 3D by utilizing the CFD method, which is out of the scope of this study.

Fluid inertia effect inclusion of a version of the equation can be written as:

$$\frac{\partial}{R\partial\theta}\left(\frac{h^3}{\mu}\frac{\partial P}{R\partial\theta}\right)+\frac{\partial}{\partial z}\left(\frac{h^3}{\mu}\frac{\partial P}{\partial z}\right)=12\frac{\partial h}{\partial t}+\frac{\rho h^2}{\mu}\frac{\partial^2 h}{\partial t^2} \tag{2-3}$$

A pressure distribution solution can be obtained by following the stated methods above. The forces generated due to the pressure distribution can be expressed as:

$$F_r=\int_0^L\int_0^{2\pi}P(\theta,z)\cos(\theta)Rd\theta dz \tag{2-4}$$

$$F_t=\int_0^L\int_0^{2\pi}P(\theta,z)\sin(\theta)Rd\theta dz \tag{2-5}$$

2.2.1 Analytical Solution of 1D Reynolds Equation

An analytical solution of the equation is only available when the SFD can be assumed as a short-bearing assumption (SBA) or long-bearing assumption (LBA).

The short bearing assumption (SBA) is considered when the length of the damper is relatively very short with respect to the diameter of the damper. For short-length SFDs (i.e., length to diameter ratio less than 0.5, L/D<0.5), the short bearing assumption states that the oil pressure gradient along the circumferential direction is negligible with respect to the pressure gradient along the axial direction. The Reynolds equation, by including the temporal fluid inertia term, is reduced as:

$$\frac{\partial}{\partial z}\left(\frac{h^3}{\mu}\frac{\partial P}{\partial z}\right) = 12\frac{\partial h}{\partial t} + \frac{\rho h^2}{\mu}\frac{\partial^2 h}{\partial t^2} \quad (2\text{-}6)$$

The pressure distribution for the open-end boundary conditions gives:

$$P(\theta, 0) = P(\theta, L) = 0 \quad (2\text{-}7)$$

The pressure distribution for open-ended short-length SFD can be written as:

$$P(\theta, z) = \frac{6\mu}{h^3}(\dot{e}\cos(\theta) - e\dot{\theta}\sin(\theta))(z^2 - Lz) \quad (2\text{-}8)$$

The motion of the SFD journal is circular centered orbit (CCO) motion. For CCO, the radial velocity and tangential acceleration are zero. Therefore, the force generated by SFD in radial and tangential directions can be founded as:

$$F_r = -(C_{rt}V_t + M_{rr}A_r) \quad (2\text{-}9)$$

$$F_t = -\left(C_{tt}V_t + M_{tr}A_r\right) \quad (2\text{-}10)$$

Where, C_{tt}, C_{rt}, M_{rr} and M_{tr} are direct tangential damping coefficient, cross-coupled damping coefficient, direct radial mass coefficient, and cross-coupled mass coefficient, respectively. $V_t = e\omega$ and $A_r = -e\omega^2$ are tangential velocity and radial acceleration, respectively. e is the amplitude of the SFD journal motion. For the open ends short length SFD model with circular centered orbit (CCO) motion, force coefficients obtained by using π-film assumption (the extent of oil film extends over half in the circumferential direction) and 2π-film (No oil cavitation occurs) are listed in Table 2.1 [5].

Table 2.1: Short bearing assumption force coefficients

	π-film	2π-film
C_{tt}	$\frac{\pi\mu D}{4\left(1-\varepsilon^2\right)^{3/2}}\left(\frac{L}{c}\right)^3$	$\frac{\pi\mu D}{2\left(1-\varepsilon^2\right)^{3/2}}\left(\frac{L}{c}\right)^3$
C_{rt}	$\frac{\mu\varepsilon D}{4\left(1-\varepsilon^2\right)^{2}}\left(\frac{L}{c}\right)^3$	0
M_{rr}	$\frac{\pi\rho D}{24}\left(\frac{L^3}{c}\right)\left(1-2\left(1-\varepsilon^2\right)^{1/2}\right)\left(\frac{\left(1-\varepsilon^2\right)^{1/2}-1}{\varepsilon^2\left(1-\varepsilon^2\right)^{1/2}}\right)$	$\frac{\pi\rho D}{12}\left(\frac{L^3}{c}\right)\left(1-2\left(1-\varepsilon^2\right)^{1/2}\right)\left(\frac{\left(1-\varepsilon^2\right)^{1/2}-1}{\varepsilon^2\left(1-\varepsilon^2\right)^{1/2}}\right)$
M_{tr}	$-\frac{27\rho D}{140\varepsilon}\left(\frac{L^3}{c}\right)\left[2+\frac{1}{\varepsilon}\ln\left(\frac{1-\varepsilon}{1+\varepsilon}\right)\right]$	0

Where, L , D and c are length, journal diameter, and radial clearance of the SFD, respectively. ρ and μ are effective density and viscosity of the lubricant oil. $\varepsilon = e/c$, is the ratio of orbit motion amplitude to clearance of the SFD, and it is referred as the eccentricity ratio. For no oil cavitation, i.e., 2π-film assumption, direct damping and mass coefficients (C_{tt} , M_{rr}) become twice the half film cavitation coefficients, and the cross-coupled damping and mass coefficients (C_{rt}, M_{tr}) are null. The damping coefficients are proportional to the cube of length to clearance ratio and linearly proportional to the diameter of the damper. Mass coefficients are proportional to the cube of length and linearly proportional to the diameter ratio to the damper's clearance. Since the force coefficients given above depend upon the amplitude of the motion of the SFD journal, the generated forces by SFD are nonlinear. The mass and damping coefficients change with the amplitude of the motion of the SFD location.

2.2.2 Solution of 3D Reynolds Equation of SFD

2.2.2.1 Oil Film Governing Equations

The Squeeze Film Damper is assumed as finite length and open-ended, geometrical representation, journal motion, and its coordinate system are given in Figure 2.3.

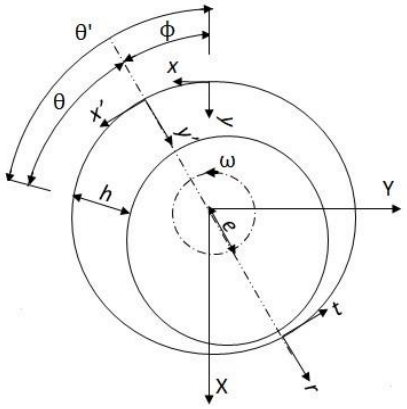

Figure 2.3. SFD geometrical presentation with the coordinate system

3-dimensional conservation of mass (Continuity) equation and conversation of momentum equation Navier-Stokes equation of fluid boundaries can be expressed as:

$$\frac{\partial \rho}{\partial x} \nabla(\rho V) = 0 \tag{2-11}$$

$$\rho\left(\frac{\partial V}{\partial t} + V.\nabla V\right) = -\nabla P + \nabla.(\mu \nabla V) + \nabla\left(-\frac{2\mu}{3}\nabla.V\right) + \rho g \tag{2-12}$$

Instantaneous pressure distribution can be solved by given equations. Simplification is performed with the following assumptions:

1. The body force terms are very small compared to the viscous, inertia, and pressure terms.

2. The fluid is Newtonian, incompressible (constant density), iso-viscous (constant viscosity), and iso-thermal flow.

Applying these assumptions and extending Eqs. (2-11) - (2-12) yields the following equations.

$$\frac{\partial u}{\partial x}+\frac{\partial v}{\partial y}+\frac{\partial w}{\partial z}=0 \tag{2-13}$$

$$\rho\left\{\frac{\partial u}{\partial t}+u\frac{\partial u}{\partial x}+v\frac{\partial u}{\partial y}+w\frac{\partial u}{\partial z}\right\}=-\frac{\partial P}{\partial x}+\mu\frac{\partial^2 u}{\partial y^2} \tag{2-14}$$

$$\rho\left\{\frac{\partial v}{\partial t}+u\frac{\partial v}{\partial x}+v\frac{\partial v}{\partial y}+w\frac{\partial v}{\partial z}\right\}=-\frac{\partial P}{\partial y}+\mu\frac{\partial^2 v}{\partial y^2} \tag{2-15}$$

$$\rho\left\{\frac{\partial w}{\partial t}+u\frac{\partial w}{\partial x}+v\frac{\partial w}{\partial y}+w\frac{\partial w}{\partial z}\right\}=-\frac{\partial P}{\partial z}+\mu\frac{\partial^2 w}{\partial y^2} \tag{2-16}$$

Furthermore, thin oil film assumption is applied such as $c << R$. Therefore, the effect of curvature and variation of the pressure across the film is negligible, i.e. $\partial P/\partial y = 0$.

Flow equations are normalized by introducing non-dimensional forms for related terms. It also determines the dependency of fluid inertia terms on the Reynolds number. Non-dimensional parameters can be given as:

$$\theta=\theta'-\phi=\frac{x}{R}-\Omega t,\ \zeta=\frac{z}{R},\ \eta=\frac{y}{c},\ \tau=\Omega t,$$

$$\bar{u}=\frac{u}{R\Omega},\ \bar{v}=\frac{v}{c\Omega},\ \bar{w}=\frac{w}{c\Omega}, \tag{2-17}$$

$$\bar{P}=\frac{Pc^2}{R^2\Omega\mu},\ \bar{F}=\frac{Fc^2}{R^4\Omega\mu},\ H=\frac{h}{c}=1+\varepsilon\cos(\theta),\ \mathrm{Re}=\frac{\rho\Omega c^2}{\mu}$$

The non-dimensional parameters expressed in Eq. (2-17) are inserted into Eqs. (2-13) - (2-16) as:

$$\frac{\partial \bar{u}}{\partial \theta}+\frac{\partial \bar{v}}{\partial \eta}+\frac{\partial \bar{w}}{\partial \zeta}=0 \tag{2-18}$$

$$\mathrm{Re}\left\{\frac{\partial \bar{u}}{\partial \tau}+\bar{u}\frac{\partial \bar{u}}{\partial \theta}+\bar{v}\frac{\partial \bar{u}}{\partial \eta}+\bar{w}\frac{\partial \bar{u}}{\partial \zeta}\right\}=-\frac{\partial \bar{P}}{\partial \theta}+\frac{\partial^2 \bar{u}}{\partial \eta^2} \tag{2-19}$$

$$\mathrm{Re}\left\{\frac{\partial \bar{w}}{\partial \tau}+\bar{u}\frac{\partial \bar{w}}{\partial \theta}+\bar{v}\frac{\partial \bar{w}}{\partial \eta}+\bar{w}\frac{\partial \bar{w}}{\partial \zeta}\right\}=-\frac{\partial \bar{P}}{\partial \zeta}+\frac{\partial^2 \bar{w}}{\partial \eta^2} \tag{2-20}$$

Boundary conditions for dimensionless velocities are defined as:

$$\begin{cases} \bar{u}=0,\bar{v}=0,\bar{w}=0 & \eta=0 \\ \bar{u}=0,\bar{v}=\dfrac{\partial H}{\partial \tau},\bar{w}=0 & \eta=H \end{cases} \tag{2-21}$$

Additionally, for open-ended SFD, boundary conditions for the pressure can be expressed as:

- The pressure is periodic in the circumferential direction, i.e. $\bar{P}(\theta,\zeta)=\bar{P}(\theta+2\pi,\zeta)$.
- At the axial ends of the damper, the pressure difference is equal to zero i.e. $\bar{P}(\theta,L/D)=\bar{P}(\theta,-L/D)=0$
- The static pressure is above the cavitation pressure, which is typically ambient.

The flow velocity components and pressure distribution are expanded with first-order perturbation, and the first order is approximated as a function of the Reynolds number:

$$\bar{u}=\bar{u}_0+\mathrm{Re}\,\bar{u}_1 \tag{2-22}$$

$$\bar{v}=\bar{v}_0+\mathrm{Re}\,\bar{v}_1 \tag{2-23}$$

$$\bar{w}=\bar{w}_0+\mathrm{Re}\,\bar{w}_1 \tag{2-24}$$

$$\bar{P}=\bar{P}_0+\mathrm{Re}\,\bar{P}_1 \tag{2-25}$$

These equations indicate that velocity components and pressure distribution are split into terms that neglect inertia as zeroth order and inertial correction term as the first order. Substituting Eqs. (2-22) - (2-25) into Eqs. (2-18) - (2-20) yields:

$$-\mathrm{Re}\left[\frac{\partial \bar{u}_1}{\partial \theta}+\frac{\partial \bar{v}_1}{\partial \eta}+\frac{\partial \bar{w}_1}{\partial \zeta}\right]=\frac{\partial \bar{u}_0}{\partial \theta}+\frac{\partial \bar{v}_0}{\partial \eta}+\frac{\partial \bar{w}_0}{\partial \zeta} \tag{2-26}$$

$$\mathrm{Re}\left[\frac{\partial \bar{u}_0}{\partial \tau}+\bar{u}\frac{\partial \bar{u}_0}{\partial \theta}+\bar{v}\frac{\partial \bar{u}_0}{\partial \eta}+\bar{w}\frac{\partial \bar{u}_0}{\partial \zeta}+\frac{\partial \bar{P}_1}{\partial \theta}-\frac{\partial^2 \bar{u}_1}{\partial \eta^2}\right]=-\frac{\partial \bar{P}_0}{\partial \theta}+\frac{\partial^2 \bar{u}_0}{\partial \eta^2} \tag{2-27}$$

$$\mathrm{Re}\left[\frac{\partial \bar{w}_0}{\partial \tau}+\bar{u}\frac{\partial \bar{w}_0}{\partial \theta}+\bar{v}\frac{\partial \bar{w}_0}{\partial \eta}+\bar{w}\frac{\partial \bar{w}_0}{\partial \zeta}+\frac{\partial \bar{P}_1}{\partial \zeta}-\frac{\partial^2 \bar{w}_1}{\partial \eta^2}\right]=-\frac{\partial \bar{P}_0}{\partial \zeta}+\frac{\partial^2 \bar{w}_0}{\partial \eta^2} \tag{2-28}$$

According to only viscous continuity and momentum equations, the right-hand side of Eqs. (2-26) - (2-28) are equal to zero. Then, they can be expressed as:

$$\frac{\partial \bar{u}_0}{\partial \theta}+\frac{\partial \bar{v}_0}{\partial \eta}+\frac{\partial \bar{w}_0}{\partial \zeta}=0 \tag{2-29}$$

$$-\frac{\partial \bar{P}_0}{\partial \theta}+\mu\frac{\partial^2 \bar{u}_0}{\partial \eta^2}=0 \tag{2-30}$$

$$-\frac{\partial \bar{P}_0}{\partial \zeta}+\frac{\partial^2 \bar{w}_0}{\partial \eta^2}=0 \tag{2-31}$$

Boundary conditions for velocity components in Eqs. (2-29) - (2-31) can be given as:

$$\begin{cases} \bar{u}_0=0, \bar{v}_0=0, \bar{w}_0=0 & \eta=0 \\ \bar{u}_0=0, \bar{v}_0=\dfrac{\partial H}{\partial \tau}, \bar{w}_0=0 & \eta=H \end{cases} \tag{2-32}$$

Zeroth-order velocity components and pressure distribution can be calculated by integrating Eqs. (2-29) - (2-31) with boundary conditions given in Eq (2-32) :

$$\begin{cases} \bar{u}_0(\theta,\eta,\zeta)=\dfrac{1}{2}\dfrac{\partial \bar{P}_0}{\partial \theta}(\eta^2-\eta H) \\ \bar{w}_0(\theta,\eta,\zeta)=\dfrac{1}{2}\dfrac{\partial \bar{P}_0}{\partial \zeta}(\eta^2-\eta H) \\ \bar{v}_0(\theta,\eta,\zeta)=-\dfrac{1}{2}\left[\left(\dfrac{\partial^2 \bar{P}_0}{\partial \theta^2}+\dfrac{\partial^2 \bar{P}_0}{\partial \zeta^2}\right)\left(\dfrac{\eta^3}{3}-H\dfrac{\eta^2}{2}\right)-\dfrac{\partial \bar{P}_0}{\partial \theta}\dfrac{\partial H}{\partial \theta}\dfrac{\eta^2}{2}\right] \end{cases} \tag{2-33}$$

The Reynolds equation can be written for viscous only pressure distribution:

$$\frac{\partial}{\partial\theta}\left(H^3\frac{\partial\bar{P}_0}{\partial\theta}\right)+\frac{\partial}{\partial\zeta}\left(H^3\frac{\partial\bar{P}_0}{\partial\zeta}\right)=12\frac{\partial H}{\partial\tau} \tag{2-34}$$

First-order perturbation equations can be expressed as:

$$\frac{\partial\bar{u}_1}{\partial\theta}+\frac{\partial\bar{v}_1}{\partial\eta}+\frac{\partial\bar{w}_1}{\partial\zeta}=0 \tag{2-35}$$

$$\frac{\partial\bar{u}_0}{\partial\tau}+\bar{u}_0\frac{\partial\bar{u}_0}{\partial\theta}+\bar{v}_0\frac{\partial\bar{u}_0}{\partial\eta}+\bar{w}_0\frac{\partial\bar{u}_0}{\partial\zeta}=-\frac{\partial\bar{P}_1}{\partial\theta}+\frac{\partial^2\bar{u}_1}{\partial\eta^2} \tag{2-36}$$

$$\frac{\partial\bar{w}_0}{\partial\tau}+\bar{u}_0\frac{\partial\bar{w}_0}{\partial\theta}+\bar{v}_0\frac{\partial\bar{w}_0}{\partial\eta}+\bar{w}_0\frac{\partial\bar{w}_0}{\partial\zeta}=-\frac{\partial\bar{P}_1}{\partial\zeta}+\frac{\partial^2\bar{w}_1}{\partial\eta^2} \tag{2-37}$$

Boundary conditions for velocity components of first-order terms:

$$\begin{cases}\bar{u}_1=0,\bar{v}_1=0,\bar{w}_1=0 & \eta=0\\ \bar{u}_1=0,\bar{v}_1=0,\bar{w}_1=0 & \eta=H\end{cases} \tag{2-38}$$

Viscous (zeroth order) velocity components given in Eq (2-33) are substituted into Eq. (2-36) and Eq. (2-37), then inertial (first order) velocity components can be expressed as:

$$\begin{aligned}\bar{u}_1=&\left(\frac{\eta^2-H\eta}{2}\right)\frac{\partial\bar{P}_1}{\partial\theta}-\frac{\partial\bar{P}_0}{\partial\theta}\frac{\partial H}{\partial\tau}\left(\frac{\eta^6}{15H^3}-\frac{\eta^5}{5H^2}+\frac{\eta^4}{8H}+\frac{\eta^3}{12}-\frac{3H\eta^2}{40}\right)\\&+\left(\frac{\partial\bar{P}_0}{\partial\theta}\right)^2\frac{\partial H}{\partial\theta}\left(\frac{\eta^6}{60H}-\frac{\eta^5}{20}+\frac{\eta^4H}{24}-\frac{H^4\eta}{120}\right)+\frac{\partial^2\bar{P}_0}{\partial\tau\partial\theta}\left(\frac{\eta^3}{24}-\frac{\eta^3H}{12}+\frac{H^3\eta}{24}\right)\\&+\left(\frac{\partial\bar{P}_0}{\partial\theta}\frac{\partial^2\bar{P}_0}{\partial\theta^2}+\frac{\partial^2\bar{P}_0}{\partial\tau\partial\zeta}\frac{\partial\bar{P}_0}{\partial\zeta}\right)\left(\frac{\eta^6}{120}-\frac{\eta^5H}{40}+\frac{\eta^4H^2}{48}-\frac{H^5\eta}{240}\right)\end{aligned} \tag{2-39}$$

$$\begin{aligned}\bar{w}_1=&\left(\frac{\eta^2-H\eta}{2}\right)\frac{\partial\bar{P}_1}{\partial\zeta}-\frac{\partial\bar{P}_0}{\partial\zeta}\frac{\partial H}{\partial\tau}\left(\frac{\eta^6}{15H^3}-\frac{\eta^5}{5H^2}+\frac{\eta^4}{8H}+\frac{\eta^3}{12}-\frac{3H\eta^2}{40}\right)\\&+\frac{\partial\bar{P}_0}{\partial\theta}\frac{\partial\bar{P}_0}{\partial\zeta}\frac{\partial H}{\partial\theta}\left(\frac{\eta^6}{60H}-\frac{\eta^5}{20}+\frac{\eta^4H}{24}-\frac{H^4\eta}{120}\right)+\frac{\partial^2\bar{P}_0}{\partial\tau\partial\zeta}\left(\frac{\eta^3}{24}-\frac{\eta^3H}{12}+\frac{H^3\eta}{24}\right)\\&+\left(\frac{\partial\bar{P}_0}{\partial\theta}\frac{\partial^2\bar{P}_0}{\partial\theta^2}+\frac{\partial^2\bar{P}_0}{\partial\tau\partial\zeta}\frac{\partial\bar{P}_0}{\partial\zeta}\right)\left(\frac{\eta^6}{120}-\frac{\eta^5H}{40}+\frac{\eta^4H^2}{48}-\frac{H^5\eta}{240}\right)\end{aligned} \tag{2-40}$$

Eq. (2-35) is integrated along the film thickness by applying boundary conditions of velocity components to eliminate radial velocity components:

$$\frac{\partial}{\partial\theta}\left(\int_0^H \bar{u}_1 d\eta\right)+\frac{\partial}{\partial\zeta}\left(\int_0^H \bar{w}_1 d\eta\right)=0 \tag{2-41}$$

Inertial (first order) pressure distribution is determined by substituting Eqs. (2-39) and (2-40) into Eq. (2-41) :

$$\begin{aligned}
&\frac{\partial}{\partial\theta}\left(H^3\frac{\partial\bar{P}_1}{\partial\theta}\right)+\frac{\partial}{\partial\zeta}\left(H^3\frac{\partial\bar{P}_1}{\partial\zeta}\right)=\\
&\frac{\partial}{\partial\theta}\left\{-\frac{3H^7}{560}\frac{\partial}{\partial\theta}\left[\left(\frac{\partial\bar{P}_0}{\partial\theta}\right)^2+\left(\frac{\partial\bar{P}_0}{\partial\zeta}\right)^2\right]-\frac{3H^6}{140}\frac{\partial H}{\partial\theta}\left(\frac{\partial\bar{P}_0}{\partial\theta}\right)^2+\frac{13H^4}{70}\frac{\partial H}{\partial\tau}\frac{\partial\bar{P}_0}{\partial\theta}+\frac{\partial^2\bar{P}_0}{\partial\tau\partial\theta}\left(\frac{H^5}{10}\right)\right\}\\
&+\frac{\partial}{\partial\zeta}\left\{-\frac{3H^7}{560}\frac{\partial}{\partial\zeta}\left[\left(\frac{\partial\bar{P}_0}{\partial\theta}\right)^2+\left(\frac{\partial\bar{P}_0}{\partial\zeta}\right)^2\right]-\frac{3H^6}{140}\frac{\partial H}{\partial\theta}\frac{\partial\bar{P}_0}{\partial\theta}\frac{\partial\bar{P}_0}{\partial\zeta}+\frac{13H^4}{70}\frac{\partial H}{\partial\tau}\frac{\partial\bar{P}_0}{\partial\zeta}+\frac{\partial^2\bar{P}_0}{\partial\tau\partial\theta}\left(\frac{H^5}{10}\right)\right\}
\end{aligned} \tag{2-42}$$

Eq. (2-42)is a Reynolds-like equation for inertial (first order) pressure distribution. The Viscous (zeroth order) pressure field can be calculated from Eq.(2-34). The total oil film pressure field could be obtained using Eq.(2-25). Finally, dimensionless radial and tangential forces can be determined by integration of total pressure field over damper journal surface:

$$\begin{bmatrix}\bar{F}_r\\ \bar{F}_t\end{bmatrix}=\int_{-L/D}^{L/D}\int_{\theta_1}^{\theta_2}\bar{P}(\theta,\zeta)\begin{bmatrix}\cos(\theta)\\ \sin(\theta)\end{bmatrix}d\theta d\zeta \tag{2-43}$$

Where, θ_1 and θ_2 are the positive side of the pressure distribution.

2.2.2.2 Oil Film Pressure Field Solution

The Finite Difference Method (FDM) is utilized for the solution of the pressure field, and numerical integration of the pressure field is obtained to determine generated forces due to SFD. The usage of FDM is given in the following sections in detail.

2.2.2.2.1 Viscous(Zeroth Order) Pressure Distribution

Zeroth order pressure distribution can be found first using Eq. (2-34), then viscous pressure distribution could be substituted into a first-order pressure distribution solution. Eq. (2-34) can be expanded as:

$$\left(3H^2\frac{\partial H}{\partial\theta}\frac{\partial\bar{P}_0}{\partial\theta}+H^3\frac{\partial^2\bar{P}_0}{\partial\theta^2}\right)+\left(H^3\frac{\partial^2\bar{P}_0}{\partial\zeta^2}\right)=12\frac{\partial H}{\partial\tau} \tag{2-44}$$

Where partial derivate terms related to film thickness, H can be expressed assuming CCO motion by using the definition given in Eq. (2-17):

$$\begin{aligned}\frac{\partial H}{\partial\theta}&=-\varepsilon\sin(\theta)\\ \frac{\partial H}{\partial\tau}&=\varepsilon\sin(\theta)\end{aligned} \tag{2-45}$$

Partial differential terms related to pressure distribution can be expanded by means of FDM and expressed as:

$$\begin{aligned}\frac{\partial\bar{P}}{\partial\theta}&=\frac{\bar{P}(\theta,\zeta)-\bar{P}(\theta-\Delta\theta,\zeta)}{\Delta\theta}=\frac{\bar{P}_{i,j}-\bar{P}_{i-1,j}}{\Delta\theta}\\ \frac{\partial\bar{P}}{\partial\zeta}&=\frac{\bar{P}(\theta,\zeta)-\bar{P}(\theta,\zeta-\Delta\zeta)}{\Delta\zeta}=\frac{\bar{P}_{i,j}-\bar{P}_{i,j-1}}{\Delta\zeta}\\ \frac{\partial^2\bar{P}}{\partial\theta^2}&=\frac{\bar{P}(\theta+\Delta\theta,\zeta)-2\bar{P}(\theta,\zeta)+\bar{P}(\theta-\Delta\theta,\zeta)}{\partial\theta^2}\\ &=\frac{\bar{P}_{i+1,j}-2\bar{P}_{i,j}+\bar{P}_{i-1,j}}{\Delta\theta^2}\\ \frac{\partial^2\bar{P}}{\partial\zeta^2}&=\frac{\bar{P}(\theta,\zeta+\Delta\zeta)-2\bar{P}(\theta,\zeta)+\bar{P}(\theta,\zeta-\Delta\zeta)}{\partial\zeta^2}\\ &=\frac{\bar{P}_{i,j+1}-2\bar{P}_{i,j}+\bar{P}_{i,j-1}}{\Delta\zeta^2}\end{aligned} \tag{2-46}$$

After definitions of partial derivatives, Eq. (2-44) can be solved for zeroth order pressure grid [35]:

$$\bar{P}_{0_{i,j}} = \frac{A_4 + \left[A_1 + A_2\right]\bar{P}_{0_{i-1,j}} + A_2\bar{P}_{0_{i+1,j}} + A_3\left(\bar{P}_{0_{i,j+1}} - \bar{P}_{0_{i,j-1}}\right)}{\left[A_1 + 2A_2 + 2A_3\right]} \tag{2-47}$$

Where,

$$\begin{aligned} A_1 &= \frac{-3H_i^{\,2}\left(\varepsilon\sin(\theta_i)\right)}{\Delta\theta} \\ A_2 &= -\frac{H_i^{\,3}}{\Delta\theta^2} \\ A_3 &= -\frac{H_i^{\,3}}{\Delta\zeta^2} \\ A_4 &= 12\varepsilon\sin(\theta_i) \end{aligned} \tag{2-48}$$

2.2.2.2.2 Inertial (First Order) Pressure Distribution

First order pressure distribution can be solved by using Eq. (2-44), and it can be expanded as:

$$H^3\frac{\partial^2\bar{P}_1}{\partial\theta^2} + 3H^2\frac{\partial H}{\partial\theta}\frac{\partial\bar{P}_1}{\partial\theta} + H^3\frac{\partial^2\bar{P}_1}{\partial\zeta^2} = 12\frac{\partial H}{\partial\tau} + G_1(\theta,\zeta) + G_2(\theta,\zeta) \tag{2-49}$$

Where,

$$
\begin{aligned}
G_1(\theta,\zeta) &= -\frac{3H^7}{280}\left[\left(\frac{\partial^2\bar{P}_0}{\partial\theta^2}\right)^2+\frac{\partial\bar{P}_0}{\partial\theta}\frac{\partial^3\bar{P}_0}{\partial\theta^3}+\left(\frac{\partial^2\bar{P}_0}{\partial\theta\partial\zeta}\right)^2+\frac{\partial\bar{P}_0}{\partial\zeta}\frac{\partial^3\bar{P}_0}{\partial\theta^2\partial\zeta}\right] \\
&-\frac{3H^6}{40}\frac{\partial H}{\partial\theta}\left[\frac{\partial\bar{P}_0}{\partial\theta}\frac{\partial^2\bar{P}_0}{\partial\theta^2}+\frac{\partial\bar{P}_0}{\partial\theta}\frac{\partial^2\bar{P}_0}{\partial\theta\partial\zeta}\right] \\
&-\frac{9H^5}{70}\left(\frac{\partial H}{\partial\theta}\right)^2\left(\frac{\partial\bar{P}_0}{\partial\theta}\right)^2-\frac{3H^6}{140}\frac{\partial^2 H}{\partial\theta^2}\left(\frac{\partial\bar{P}_0}{\partial\theta}\right)^2-\frac{3H^6}{70}\frac{\partial H}{\partial\theta}\frac{\partial\bar{P}_0}{\partial\theta}\frac{\partial^2\bar{P}_0}{\partial\theta^2} \\
&+\frac{26H^3}{35}\frac{\partial H}{\partial\theta}\frac{\partial H}{\partial\tau}\frac{\partial\bar{P}_0}{\partial\theta}+\frac{13H^4}{70}\frac{\partial^2 H}{\partial\tau\partial\theta}\frac{\partial\bar{P}_0}{\partial\theta}+\frac{13H^4}{70}\frac{\partial H}{\partial\tau}\frac{\partial^2\bar{P}_0}{\partial\theta^2} \\
&\frac{\partial^3\bar{P}_0}{\partial\tau\partial\theta^2}\left(\frac{H^5}{10}\right)+\frac{\partial^2\bar{P}_0}{\partial\tau\partial\theta}\left(\frac{H^4}{2}\right)\frac{\partial H}{\partial\theta}
\end{aligned}
\tag{2-50}
$$

$$
\begin{aligned}
G_2(\theta,\zeta) &= -\frac{3H^7}{280}\left[\left(\frac{\partial^2\bar{P}_0}{\partial\theta\partial\zeta}\right)^2+\frac{\partial\bar{P}_0}{\partial\theta}\frac{\partial^3\bar{P}_0}{\partial\theta\partial\zeta^2}+\left(\frac{\partial^2\bar{P}_0}{\partial\zeta^2}\right)^2+\frac{\partial\bar{P}_0}{\partial\zeta}\frac{\partial^3\bar{P}_0}{\partial\zeta^3}\right] \\
&-\frac{3H^6}{140}\frac{\partial H}{\partial\theta}\left[\frac{\partial^2\bar{P}_0}{\partial\theta\partial\zeta}\frac{\partial\bar{P}_0}{\partial\zeta}+\frac{\partial\bar{P}_0}{\partial\theta}\frac{\partial^2\bar{P}_0}{\partial\zeta^2}\right] \\
&+\frac{H^5}{10}\frac{\partial^3\bar{P}_0}{\partial\tau\partial\zeta^2}+\frac{13H^4}{70}\frac{\partial H}{\partial\tau}\frac{\partial^2\bar{P}_0}{\partial\zeta^2}
\end{aligned}
\tag{2-51}
$$

Fourth ad higher partial differential terms are neglected, and the chain rule $\frac{\partial}{\partial\tau}=\frac{\partial}{\partial\theta}\frac{\partial\theta}{\partial\tau}=-\frac{\partial}{\partial\theta}$ is used. Higher order finite differences and mixed derivatives are written as:

$$\frac{\partial^3 \bar{P}}{\partial \theta^3} = \frac{\bar{P}(\theta+2\Delta\theta,\zeta) - 2\bar{P}(\theta+\Delta\theta,\zeta) + 2\bar{P}(\theta-\Delta\theta,\zeta) - \bar{P}(\theta-2\Delta\theta,\zeta)}{2\Delta\theta^3}$$
$$= \frac{\bar{P}_{i+2,j} - 2\bar{P}_{i+1,j} + \bar{P}_{i-1,j} - \bar{P}_{i-2,j}}{2\Delta\theta^3}$$
$$\frac{\partial^3 \bar{P}}{\partial \zeta^3} = \frac{\bar{P}(\theta,\zeta+2\Delta\zeta) - 2\bar{P}(\theta,\zeta+\Delta\zeta) + 2\bar{P}(\theta,\zeta-\Delta\zeta) - \bar{P}(\theta,\zeta-2\Delta\zeta)}{2\Delta\zeta^3}$$
$$= \frac{\bar{P}_{i,j+2} - 2\bar{P}_{i,j+1} + \bar{P}_{i,j-1} - \bar{P}_{i,j-1}}{2\Delta\zeta^3}$$
$$\frac{\partial^2 \bar{P}}{\partial\theta\partial\zeta} = \frac{\bar{P}(\theta,\zeta) - \bar{P}(\theta-\Delta\theta,\zeta) - \bar{P}(\theta,\zeta-\Delta\zeta) + \bar{P}(\theta-\Delta\theta,\zeta-\Delta\zeta)}{\Delta\theta\Delta\zeta}$$
$$= \frac{\bar{P}_{i,j} - \bar{P}_{i-1,j} - \bar{P}_{i,j-1} + \bar{P}_{i-1,j-1}}{\Delta\theta\Delta\zeta}$$
$$\frac{\partial^3 \bar{P}}{\partial\theta\partial\zeta^2} = \frac{\bar{P}(\theta,\zeta+\Delta\zeta) - 2\bar{P}(\theta,\zeta) + \bar{P}(\theta,\zeta-\Delta\zeta)}{\Delta\theta\Delta\zeta^2}$$
$$+ \frac{-\bar{P}(\theta-\Delta\theta,\zeta+\Delta\zeta) - 2\bar{P}(\theta-\Delta\theta,\zeta) + \bar{P}(\theta-\Delta\theta,\zeta-\Delta\zeta)}{\Delta\theta\Delta\zeta^2}$$
$$= \frac{\bar{P}_{i,j+1} - 2\bar{P}_{i,j} - \bar{P}_{i,j-1} + 2\bar{P}_{i-1,j} - \bar{P}_{i-1,j-1}}{\Delta\theta\Delta\zeta^2}$$
$$\frac{\partial^3 \bar{P}}{\partial\theta^2\partial\zeta} = \frac{\bar{P}(\theta+\Delta\theta,\zeta) - 2\bar{P}(\theta,\zeta) + \bar{P}(\theta-\Delta\theta,\zeta)}{\Delta\theta^2\Delta\zeta}$$
$$+ \frac{-\bar{P}(\theta+\Delta\theta,\zeta-\Delta\zeta) + 2\bar{P}(\theta,\zeta-\Delta\zeta) - \bar{P}(\theta-\Delta\theta,\zeta-\Delta\zeta)}{\Delta\theta^2\Delta\zeta}$$
$$= \frac{\bar{P}_{i+1,j} - 2\bar{P}_{i,j} + \bar{P}_{i-1,j} - \bar{P}_{i+1,j-1} + 2\bar{P}_{i,j-1} - \bar{P}_{i-1,j-1}}{\Delta\theta^2\Delta\zeta} \quad (2\text{-}52)$$

After the definition of partial derivate representation in FDM, Eq. (2-49) can be solved for first order pressure grid [35]:

$$\bar{P}_{1_{i,j}} = \frac{\left[A_4 + G_{1_{i,j}} + G_{2_{i,j}}\right] + \left[A_1 + A_2\right]\bar{P}_{1_{i-1,j}} + A_2\bar{P}_{1_{i+1,j}} + A_3\left(\bar{P}_{1_{i,j+1}} - \bar{P}_{1_{i,j-1}}\right)}{\left[A_1 + 2A_2 + 2A_3\right]} \quad (2\text{-}53)$$

2.2.2.3 Oil Film Generated Force Solution

Tangential and radial forces are obtained similarly as FDM, Eq. (2-44) can be expressed as:

$$\begin{bmatrix} \bar{F}_r \\ \bar{F}_t \end{bmatrix} = \sum_{i=1}^{N} \sum_{j=1}^{M} \bar{P}_{i,j} \begin{bmatrix} \cos(\theta_i) \\ \sin(\theta_i) \end{bmatrix} \Delta\theta \Delta\zeta \tag{2-54}$$

Where M and N are the number of grid that divides θ and ζ coordinates, respectively. These determined non-dimensional tangential and radial forces are in the form given in Eq. (2-17).

Dimensional radial and tangential forces are expressed as:

$$\begin{aligned} F_r &= \bar{F}_r \frac{\mu \Omega R^4}{c^2} \\ F_t &= \bar{F}_t \frac{\mu \Omega R^4}{c^2} \end{aligned} \tag{2-55}$$

By assuming Circular Centered Orbit (CCO) motion assumption, the transformation of fluid film reaction forces into fixed inertial coordinates, i.e. *{X, Y}* can be obtained as:

$$\begin{aligned} K_{SFD,eq} &= F_r \big/ (\varepsilon c) \\ C_{SFD,eq} &= F_t \big/ (\Omega \varepsilon c) \end{aligned} \tag{2-56}$$

Then,

$$\begin{aligned} f_{n,x} &= K_{SFD,eq} x + C_{SFD,eq} \dot{x} \\ f_{n,y} &= K_{SFD,eq} y + C_{SFD,eq} \dot{y} \end{aligned} \tag{2-57}$$

These forces are nonlinear forces generated by SFD in X and Y directions.

2.2.3 Neural Network Simulation Model for SFD

The solution of pressure distribution of SFD with FDM is accurate for the wide range of geometrical parameters of SFD and the wide range of used oil's fluid parameters. Furthermore, the inertia effect of oil can be included with the help of described first-order perturbation solution of 3D flow equations. In nonlinear vibration problem,

plenty of generated nonlinear force solution which needs pressure distribution solution is required for iterations. However, the FDM solution of the pressure field is computationally cost. Therefore, the Neural Network simulation model is performed to obtain a simulation model for non-dimensional SFD parameters inputs and non-dimensional SFD generated forces outputs. Once the accurate network is developed, the simulation model can be efficiently used for various parameters of SFD in design and analysis processes.

Plenty of parameter inputs for generated forces due to SFD are reduced using non-dimensional parameters given in Eq. (2-17). Necessary inputs and outputs for neural network simulation of SFD and inputs' range for this study are shown in Table 2.2.

Table 2.2 Network Simulation Inputs and Outputs

	Inputs	**Description**	**Range**
1	ε	Eccentricity ratio (e/c)	$0<\varepsilon<1$
2	L/D	Length to Diameter ratio	$0.05<L/D<1$
3	Re	Reynolds Number	$0<Re<15$
	Outputs		
1	$\overline{F_r}$	Non-dimensional Radial Force	-
2	$\overline{F_t}$	Non-dimensional Tangential Force	-

A typical neural network can be expressed with the number of layers, the number of neurons, transfer functions, and the training algorithm. A feedforward layered neural network is utilized to perform neural network simulation. After sensitivity studies, Hyperbolic-Tangent Sigmoid is used as a transfer function for layers except for the last layer. In the last layer, the linear transfer function is utilized. Minimizing MSE is an objective function by tuning bias vectors and weight matrices. The Levenberg-Marquardt algorithm is used as a training function in neural network simulations.

27000 input data set is run using FDM to obtain output data set for training and testing Neural Network simulations. Two different network study is performed using

MATLAB Neural Network toolbox with the different number of hidden layer and neurons for comparison purposes. A description of these neural network studies is given in Table 2.3.

Table 2.3 Description of Networks

Network	**Hidden Layer**	**Neuron**	**Performance (MSE)**	**Epoch**	**Time (%)**
A	*2*	*12-144*	*4.2E-04*	*150*	*30%*
B	*3*	*12-144-12*	*3.2E-05*	*150*	*%100 (13 min)*

CHAPTER 3

NONLINEAR SOLUTION METHODS

After obtaining the equation of motion for linear rotordynamic system and nonlinear forcing term generated by SFD with described mathematical modeling in the previous chapter, Harmonic Balance Method (HBM) is utilized for transforming nonlinear differential equations into nonlinear algebraic equations. Receptance Method (RM) is used to reduce the number of nonlinear equations. The final nonlinear equations are solved with Newton's Method with Arc-length Continuation. This chapter describes these methods for nonlinear vibrations of the rotor-bearing system supported by SFD.

3.1 Harmonic Balance Method

HBM is one of the most powerful and widely used method in the analysis of nonlinear vibratory systems to obtain a steady-state response in the frequency domain. The fundamental of the concept is that the response would be periodic if the system is excited periodically. Fourier series is utilized to represent both the excitation forcing term and the response. The primary goal of HBM is converting the nonlinear differential equations into nonlinear algebraic equations. As excitation and response terms are represented with Fourier series, time derivative terms in Equation of Motion (EOM) are converted into sine and cosine. Finally, each harmonic terms, such as sine and cosine, are equivalent separately in EOM.

The equation of motion for a rotor-bearing system supported by nonlinear SFDs can be expressed as:

$$\mathbf{M}\ddot{\mathbf{x}}(t)+(\mathbf{C}+\Omega\mathbf{G})\dot{\mathbf{x}}(t)+\mathbf{K}(1+i\eta)\mathbf{x}(t)+\mathbf{f_n}(\mathbf{x},\dot{\mathbf{x}},t)=\mathbf{f}(t) \tag{3-1}$$

Where, $\mathbf{M}$, $\mathbf{G}$, $\mathbf{C}$ and $\mathbf{K}$, matrices are mass, gyroscopic, damping, and stiffness matrices of the rotor-bearing system, respectively. η is the loss factor for structural damping. $\mathbf{f_n}$ is the nonlinear forcing vector due to SFDs. $\mathbf{f}$ is the unbalance forcing vector acting on the rotor dynamic system and $\mathbf{x}$ is the displacement vector.

Since the steady-state response is interested, for periodic forcing $\mathbf{x}(t)$ is assumed as periodic as well. Displacement response and nonlinear forcing vectors can be expressed as:

$$\mathbf{x}(t) = \mathbf{x}_0 + \sum_{p=1}^{k} \mathbf{x}_{c,p} \cos(p\omega t) + \mathbf{x}_{s,p} \sin(p\omega t) \tag{3-2}$$

$$\mathbf{f_n}(\mathbf{x}, \dot{\mathbf{x}}, t) = \mathbf{f_{n,0}} + \sum_{p=1}^{k} \mathbf{f_{nc,p}} \cos(p\omega t) + \mathbf{f_{ns,p}} \sin(p\omega t) \tag{3-3}$$

Where $\mathbf{x}_{c,p}$ and $\mathbf{x}_{s,p}$ are cosine and sine coefficients for the p^{th} harmonic displacement vector, respectively. $\mathbf{f_{nc,p}}$ and $\mathbf{f_{ns,p}}$ are the cosine and sine coefficients for the p^{th} harmonic displacement vector, respectively. ω is the base frequency showing the period, and all other frequencies given in the series are integer multiples of ω. Substituting Eq.(3-2) and Eq. (3-3) into Eq. (3-2) and applying HBM, nonlinear algebraic equations for the p^{th} harmonic can be obtained as follows:

$$\mathbf{Z}_p(\omega) \begin{pmatrix} \mathbf{x}_{c,p} \\ \mathbf{x}_{s,p} \end{pmatrix} + \mathbf{f}_{\mathbf{n},p}(\mathbf{x}, \dot{\mathbf{x}}, t) = \mathbf{f}_p \tag{3-4}$$

Where the dynamic stiffness matrix $\mathbf{Z}_p(\omega)$ is expressed as:

$$\mathbf{Z}_p(\omega) = \begin{bmatrix} \mathbf{K}(1+i\eta) - (p\omega)^2\mathbf{M} & (p\omega)(\mathbf{C}+\Omega\mathbf{G}) \\ -(p\omega)(\mathbf{C}+\Omega\mathbf{G}) & \mathbf{K}(1+i\eta) - (p\omega)^2\mathbf{M} \end{bmatrix} \tag{3-5}$$

A complete set of nonlinear algebraic equations for the rotordynamic system takes the following form:

$$\mathbf{r}(\mathbf{x},\omega) = \mathbf{Z}(\omega)\mathbf{x} + \mathbf{f_n}(\mathbf{x},\dot{\mathbf{x}},t) - \mathbf{f} = \mathbf{0} \tag{3-6}$$

Here,

$$\mathbf{Z}(\omega) = diag(\mathbf{Z}_0(\omega), \mathbf{Z}_1(\omega), ..., \mathbf{Z}_k(\omega)) \tag{3-7}$$

$$\mathbf{x} = \left[\mathbf{x}_0^{\mathbf{T}}, \mathbf{x}_{c,1}^{\mathbf{T}}, \mathbf{x}_{s,1}^{\mathbf{T}}, ..., \mathbf{x}_{c,k}^{\mathbf{T}}, \mathbf{x}_{s,k}^{\mathbf{T}} \right] \tag{3-8}$$

$$\mathbf{f_n} = \left[\mathbf{f}_{\mathbf{n},0}^{\mathbf{T}}, \mathbf{f}_{\mathbf{n}c,1}^{\mathbf{T}}, \mathbf{f}_{\mathbf{n}s,1}^{\mathbf{T}}, ..., \mathbf{f}_{\mathbf{n}c,k}^{\mathbf{T}}, \mathbf{f}_{\mathbf{n}s,k}^{\mathbf{T}} \right] \tag{3-9}$$

$$\mathbf{f} = \left[\mathbf{f}_0^{\mathbf{T}}, \mathbf{f}_{c,1}^{\mathbf{T}}, \mathbf{f}_{s,1}^{\mathbf{T}}, ..., \mathbf{f}_{c,k}^{\mathbf{T}}, \mathbf{f}_{s,k}^{\mathbf{T}} \right] \tag{3-10}$$

$\mathbf{r}(\mathbf{x},\omega)$ is the nonlinear equation vector, which is a function of $\mathbf{x}$ and ω. In this work, single harmonic representation is used in the case studies, i.e., $k=1$ in Eqs. (3-7) - (3-10).

3.2 Receptance Method

In most rotordynamic systems, nonlinear elements connected to the Degree of Freedoms (DoFs) are much less than the total number of DoFs in the system. Reduction methods are found efficient for these types of problems. Receptance Method (RM), [42-43] can be utilized to separate linear DOFs and nonlinear DoFs, i.e., a nonlinear element connected DoFs, and solve the equations separately, which allows a significant reduction in the number of nonlinear equations. It provides easiness in the aspect of time and convergence of the solution.

Single harmonic Steady-State response for Equation (3-1) can be written as:

$$\mathbf{x} + \mathbf{H} \cdot (\mathbf{f_n}(\mathbf{x}) - \mathbf{f}) = \mathbf{0} \tag{3-11}$$

Where $\mathbf{H}$ is Receptance matrix and given as:

$$\mathbf{H} = (\mathbf{K} \cdot (1 + i\eta) - (\omega^2)\mathbf{M} + i(\omega)(\Omega\mathbf{G} - \mathbf{C}))^{-1} \tag{3-12}$$

The receptance matrix includes matrix inversion. Modal reduction techniques would be beneficial for large systems to avoid large matrix inversion. Hence receptance matrix can be obtained utilizing modal reduction techniques. However, in rotordynamic systems, the gyroscopic matrix is a skew-symmetric and frequency-dependent matrix, so a quadratic eigenvalue problem solution is needed, which yields complex eigenvalue and eigenvector. Therefore, the eigenvalue problem is repeated for every frequency sweep. The equations are reordered such that nonlinear DoFs will be at the bottom, which means unknown forcing terms will be at the bottom. The equation of motion can be written as:

$$\begin{Bmatrix} \mathbf{x_l} \\ \mathbf{x_n} \end{Bmatrix} + \begin{bmatrix} \mathbf{H_{ll}} & \mathbf{H_{ln}} \\ \mathbf{H_{nl}} & \mathbf{H_{nn}} \end{bmatrix} \left(\begin{Bmatrix} \mathbf{0} \\ \mathbf{f_n(x_n)} \end{Bmatrix} - \begin{Bmatrix} \mathbf{f_l} \\ \mathbf{f_n} \end{Bmatrix} \right) = 0 \tag{3-13}$$

It is observed from equation (3-13) that the bottom side of the given equations in matrix form is to be solved nonlinearly first. The bottom side of the equation can be written as:

$$\mathbf{r}(\mathbf{x_n}, \omega) = \mathbf{x_n} + \mathbf{H_{nn}} \cdot \mathbf{f_n(x_n)} - \begin{bmatrix} \mathbf{H_{nl}} & \mathbf{H_{nn}} \end{bmatrix} \cdot \begin{Bmatrix} \mathbf{f_l} \\ \mathbf{f_n} \end{Bmatrix} = 0 \tag{3-14}$$

Afterward, the displacement of linear DoFs will be solved with known nonlinear forcing and known nonlinear displacement vectors by using Eq. (3-13). This indicated separation shows that the number of nonlinear equations is twice the number of nonlinear DoFs as sine and cosine terms coefficients are solved separately. If the receptance method is not used, the number of nonlinear equations would be twice the number of total DoFs in the system. Therefore, the nonlinear equation vector given in Eq. (3-6) is reduced to expressed in Eq. (3-14).

3.3 Newton's Method With Arclength Continuation

Newton's method is a widely used solution method for nonlinear vibratory systems. It uses jacobian matrices, the derivative of the equation with respect to an unknown vector. Moreover, in nonlinear systems, there may be more than one solution at a specific frequency, so the arc-length parameter should be included to follow the path even for turning points. Therefore, the described method is a nonlinear solution method with a path following.

A nonlinear SFD forcing vector can be found by described methods above, and residual equation Eq. (3-14) is obtained. Newton's Method with arc-length continuation method is used to solve nonlinear algebraic equations, which are converted by HBM. A single step of Newton's Method with Arc-length Continuation can be expressed as follows:

$$\mathbf{q}_j^{i+1} = \mathbf{q}_j^i - \begin{bmatrix} \dfrac{\partial \mathbf{r}}{\partial \mathbf{x}} & \dfrac{\partial \mathbf{r}}{\partial \omega} \\ \dfrac{\partial d}{\partial \mathbf{x}} & \dfrac{\partial d}{\partial \omega} \end{bmatrix} \begin{Bmatrix} \mathbf{r}\left(\mathbf{q}_j^i\right) \\ d\left(\mathbf{q}_j^i\right) \end{Bmatrix} \tag{3-15}$$

Here, $\mathbf{r}$ is the nonlinear equation vector which is expressed in Eq.(3-14), i is the iteration number, and j is for the j^{th} solution point. $\mathbf{q}_j^i = \left(\mathbf{x}_j^i \;\; \omega^i\right)^T$ is the vector of unknowns. d is the arc length equation defined as:

$$d\left(\mathbf{q}_j^i\right) = \Delta\mathbf{q}_j^{\mathbf{T}} \, \Delta\mathbf{q}_j - s^2 \tag{3-16}$$

Where, $\Delta\mathbf{q}_j = \mathbf{q}_j - \mathbf{q}_{j-1}$ and s is the radius of the hypothetical sphere. The details of the solution procedure can be found in [41].

CHAPTER 4

CASE STUDIES

4.1 Rotordynamic System

The rotor of a small turbojet engine [27] given in Figure 4.1 is used for the numerical case study. The rotordynamic model is developed using 18 Timoshenko beam elements (19 nodes) supported by two bearings and contains one compressor disk and one turbine disk, modeled as lumped masses and inertias. All parameters of the model are given in Table 4.1 and Table 4.2.

The first two undamped critical speeds are obtained from Campbell Diagram, shown in Figure 4.2. Critical Speeds are found as 2511 rad/s and 2726 rad/s, similar to the results in [27]. As only the first two modes are a range of interest, these two modes are studied in the case study. Corresponding mode shapes of the first two critical speeds are shown in Figure 4.3. It is observed from mode shapes, 1^{st} mode is the conical mode, and 2^{nd} mode shape is the cylindrical mode. These mode shapes explain that 1^{st} mode is affected by the gyroscopic effect more than 2^{nd} mode, which is the observation of the Campbell Diagram.

For unbalance response characteristic of the rotordynamic system, the loss factor η is taken as 0.01. Different amount of unbalance mass is located at disk 1 (4^{th} node), and nonlinear responses from disk locations are investigated in frequency response graphs. An SFD is connected to 1^{st} support (6^{th} node), and all geometrical and oil properties are given in Table 4.3.

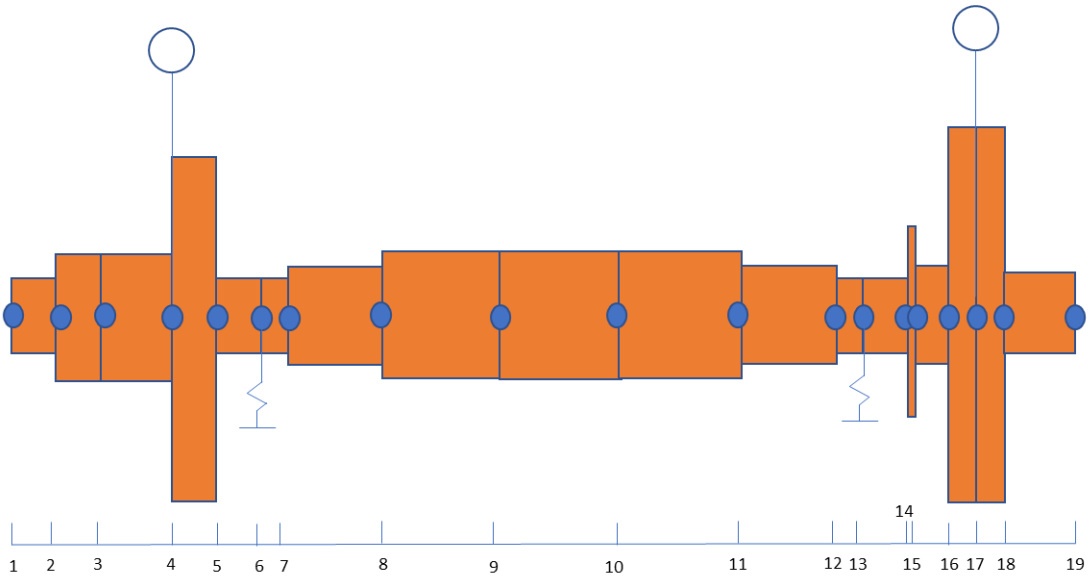

Figure 4.1: Rotor of a small Turbojet engine FEM sketch

Table 4.1: Shaft Properties

Field. #	***1***	***2***	***3***	***4***	***5***	***6***	***7***	***8***	***9***
$D\ (mm)$	12	16	16	60	8	8	13	14.5	14.5
$l(mm)$	6	9	13	10	6.5	3.5	18	17	17
$\rho\ (kg/m^3)$	7810	0	0	0			7810		
$E\ (GPa)$	210	72	72	72			210		
Field. #	***10***	***11***	***12***	***13***	***14***	***15***	***16***	***17***	***18***
$D\ (mm)$	14.5	13	8	8	20	10	60	60	10
$l(mm)$	17	18	3.5	5.5	2	3	3.8	3.7	8.5
$\rho\ (kg/m^3)$			7810				0	0	7810
$E\ (GPa)$					210				

Table 4.2: Lumped Mass & Bearing Properties

Mass #	***1***	***2***
Node #	4	17
$m(kg)$	0.0721	0.0658
$I_{polar}(kgmm^2)$	20.26	20.99
$I_{diametral}(kgmm^2)$	12.19	10.74
Bearing #	***1***	***2***
Node #	6	13
$k_{lateral}(MN/m)$	1	1
$k_{bending}(Nm/rad)$	0	0

Table 4.3: SFD Properties

SFD properties	
Connected Node	6
Geometrical Parameters	
$D\ (mm)$	20
$l(mm)$	5
$c(mm)$	0.1
Oil Parameters	
μ $(centipose)$	5.1
$\rho\ (kg/m^3)$	1000

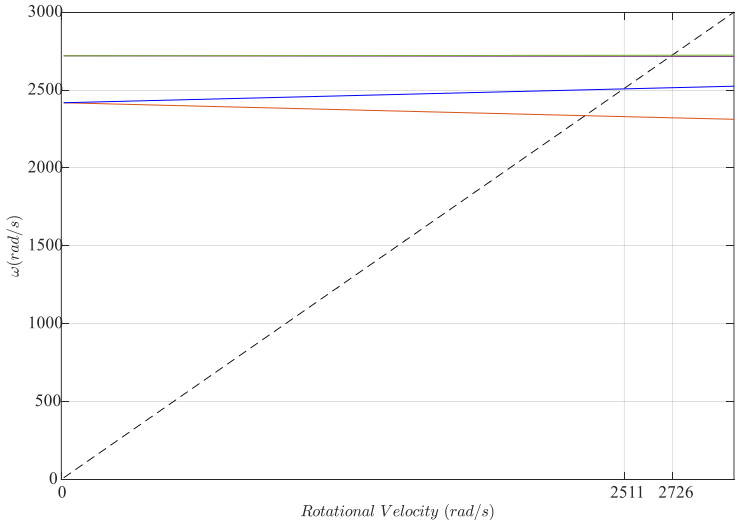

Figure 4.2. Campbell Diagram

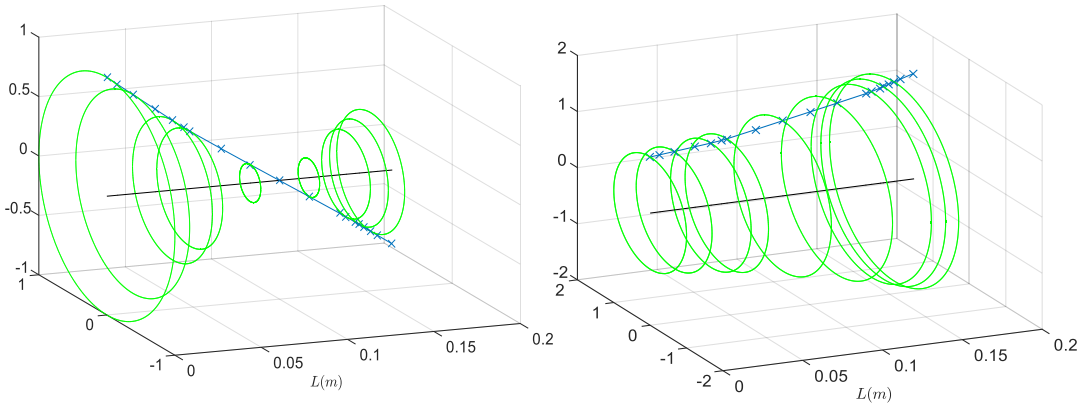

Figure 4.3. Mode Shapes

4.2 Nonlinear vibration response with the analytical solution of 1D Reynolds Equation of SFD

Analytical solution of 1D Reynolds equation of SFD is incorporated with rotordynamic model, then effects of SFD parameters and amount of unbalance loading is studied.

In the analysis, the frequency range covering the first two critical speeds is investigated. It can be clearly seen from Figure 4.4 that SFD significantly reduces the amplitudes of the vibration since it provides a nonlinear damping force. Because of the π-film oil cavitation, SFD also provides a stiffening effect and shifts the resonance frequency towards the right resulting in a hardening effect.

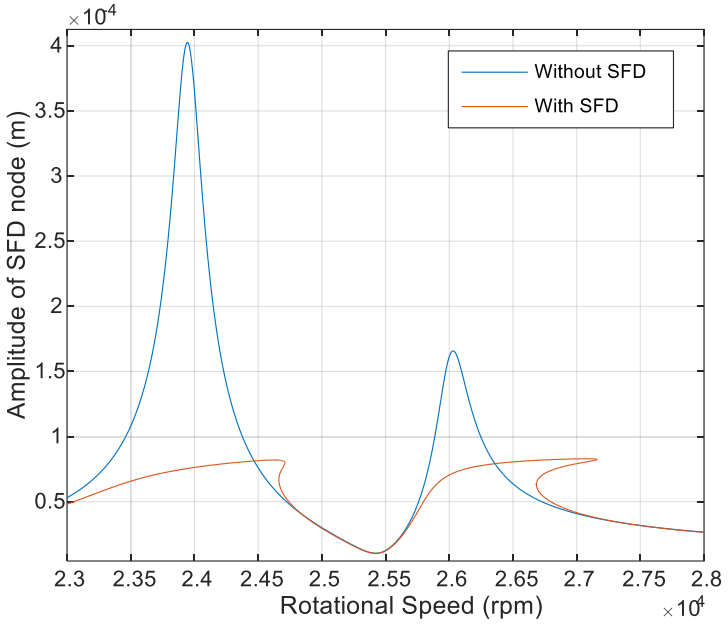

Figure 4.4: Response of 4th Node

The nonlinear response of the 4th node corresponding to the location of the first lumped mass is given in Figure 4.5 for half film cavitation and no oil cavitation. No cavitation reduces the peak vibration amplitudes, and no hardening behavior is observed due to the lack of cross-coupled damping term. Half film cavitation response shows that a hardening effect occurs, which is inherited from the presence

of cross-coupled coefficients of damping and inertia. Physically, sophisticated seal mechanisms at the SFD support are used to provide no cavitation operating conditions for the SFD; however, in reality, it may not be possible for all operating conditions. Therefore, cavitation models such as half film cavitation other than no cavitation model should be studied.

The effect of the diameter of the SFD on the nonlinear forced responses of the 4^{th} node is given in Figure 4.6. It is observed that the amplitude of the response decreases as the diameter of the SFD increases since the generated nonlinear dissipating force is proportional to the diameter of the SFD. Similarly, the shift in resonance frequency decreases slightly as the diameter increases. It should be noted that the main reason for the hardening effect is the cross-coupling terms of the SFD force, which reduces in this case.

The effect of the length of the SFD on the forced response of the 4^{th} node is presented in Figure 4.7. It is observed that the effect of length on the response is higher than the effect of the diameter as the damping capacity of SFD is proportional to the cube of the length. In contrast, it is linearly proportional to its diameter. Shorter lengths result in higher vibration amplitudes and a stiffening effect. It should be noted that the multiplication of diameter, length, and viscosity can be taken as a single parameter; however, they are investigated separately to assess their effect by changing them physically.

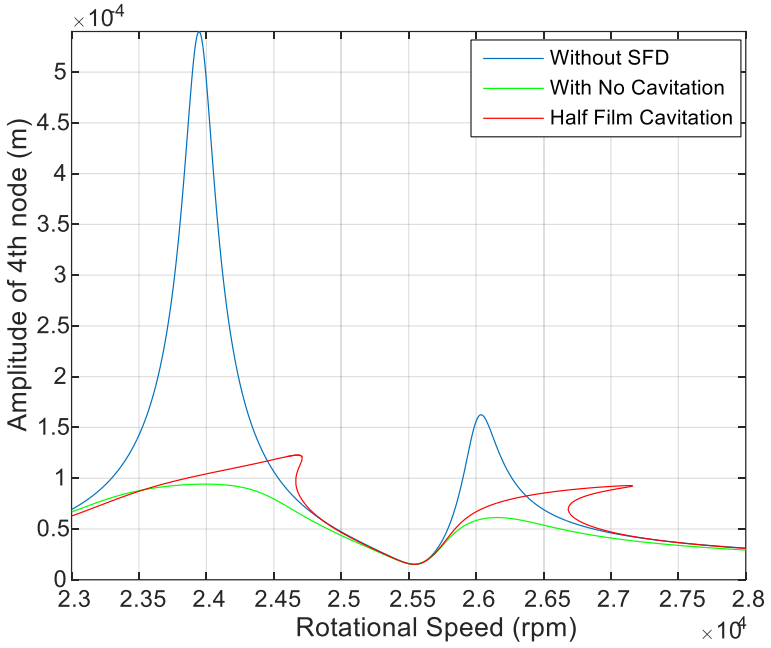

Figure 4.5: Response of 4th node for no cavitation and half film cavitation

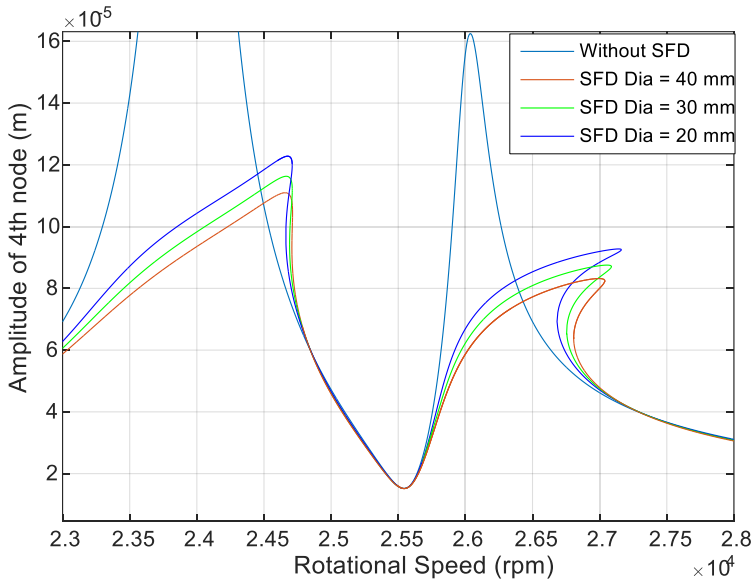

Figure 4.6: Response of 4th node for different SFD diameters

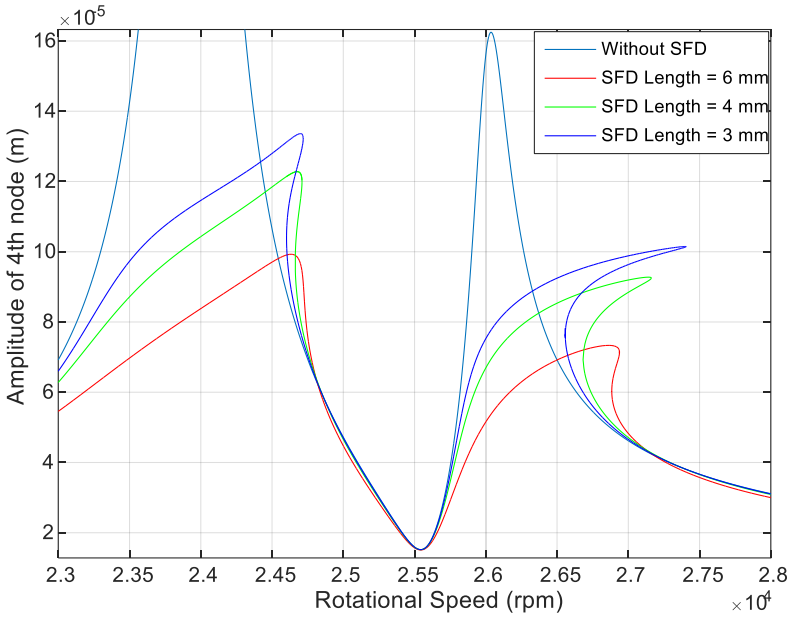

Figure 4.7: Response of 4th node for different SFD lengths

The effect of the clearance on the forced response of the 4th node is given in Figure 4.8. Results show that as the clearance value decreases, resonance amplitude decreases, and the frequency shifts increases. An interesting dynamic behavior is observed where the resonance amplitude of the second mode becomes higher than the amplitude without the SFD for a clearance value of 0.2 mm. Therefore, clearance is an essential parameter in the design of SFDs.

The effect of clearance on the forced response of the 17th node, i.e., the location of the second lumped mass, is given in Figure 4.9. Similar to the first lumped mass location, response amplitude decreases as clearance decreases. Around the 2nd mode, a more significant shift is observed for the 17th node compared to the 4th node. The maximum response amplitude at the 2nd mode for 0.2 mm clearance is almost equal to the case without SFD.

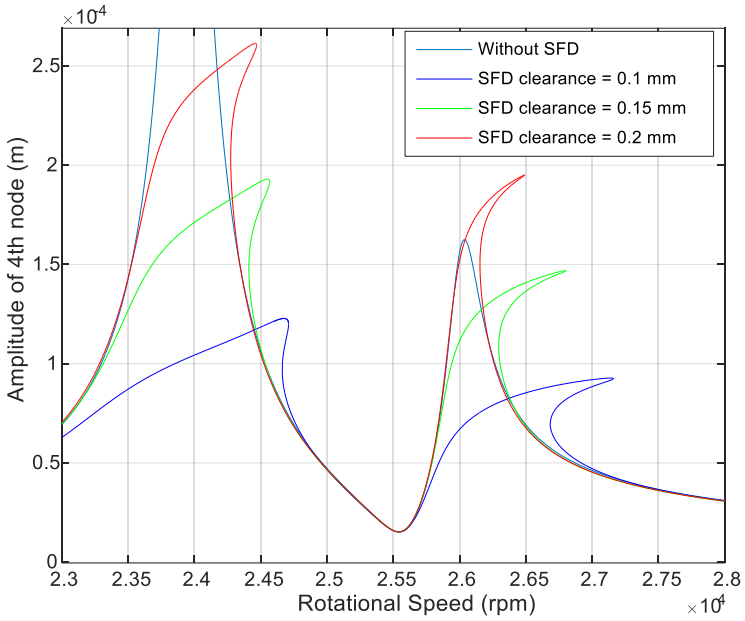

Figure 4.8: Response of 4th node for different clearance values

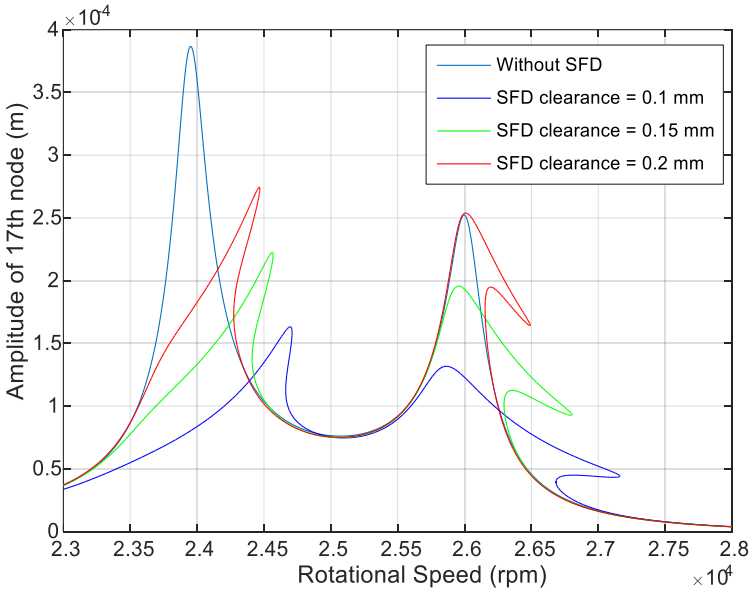

Figure 4.9: Response of 17th node for different clearance values

Normalized forced responses for the 4th node for a different amount of unbalance are given in Figure 4.10. The amount of unbalance in the system may vary due to operation conditions, manufacturing tolerances, etc. The amount of unbalance loadings are given as percentages of the base unbalance loading case; for example,

%10 of unbalance is 72.1x10^{-3} *g-mm*. As the unbalance amount increases, the response amplitude of the 4th node decreases around the 1st mode. However, around the 2nd mode, the response of %50 unbalance cases are slightly higher than the %10 unbalance cases. Resonance frequencies shift to higher frequencies as the amount of unbalance increases.

The case study is repeated by applying the unbalance to the second lumped mass location, i.e., the 17th node. The results obtained are given in Figure 4.11. It is observed that as the unbalance increases, the response amplitude of the 17th node increases around the first mode and decreases around the 2nd mode. The frequency shift around the first mode is much higher than in the previous case. This is because SFD at the 6th node is away from the unbalance location, and as a result, it cannot decrease the vibration amplitude efficiently.

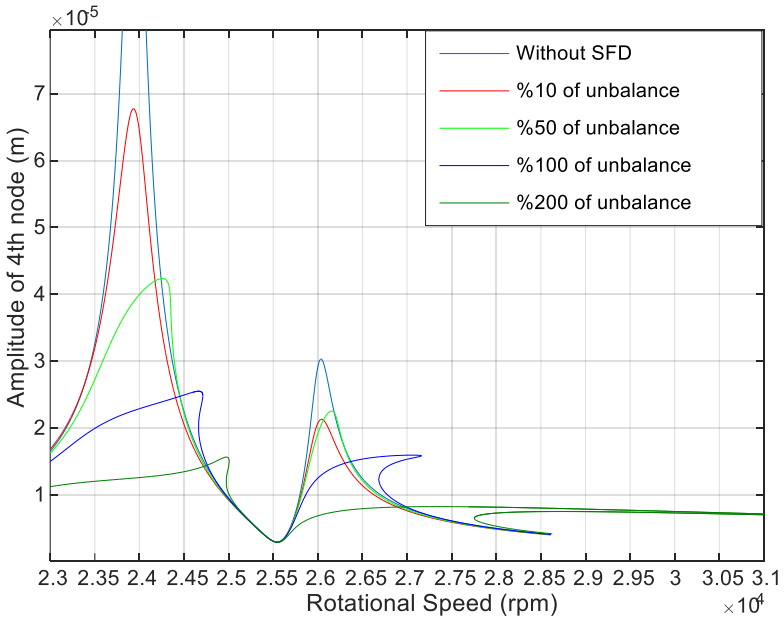

Figure 4.10: Normalized response of 4th node for a different amount of unbalance

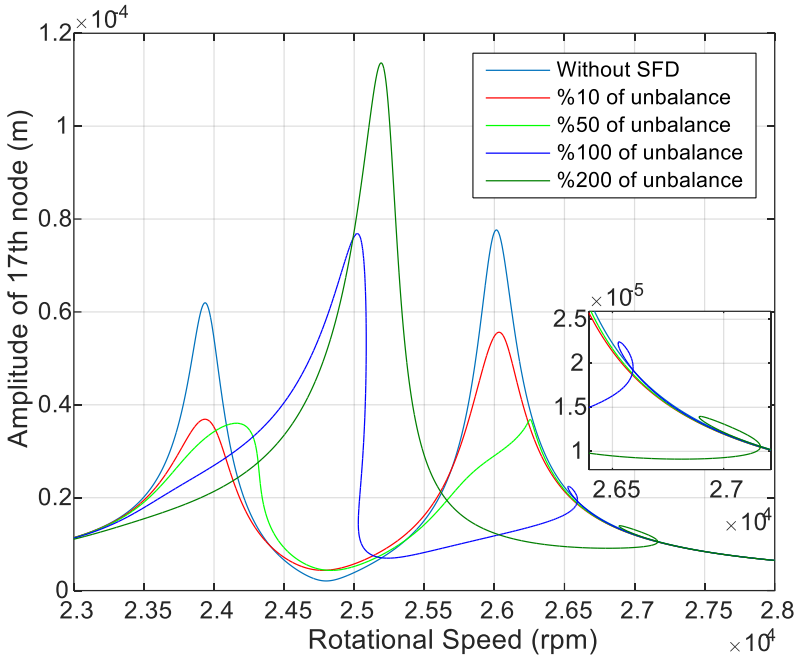

Figure 4.11: Normalized Response of 17th node for unbalance at 17th node for a different amount of unbalance

4.3 Nonlinear Vibration Response with the solution of 3D Reynolds Equation of SFD

4.3.1 Oil Film Pressure Field and Generated Force

The oil film pressure field is solved with FDM described in the mathematical modeling section. Viscous only pressure and inertial pressure fields are obtained, then their combination gives total pressure. Integration of total pressure over the journal surface domain gives force coefficients generated by SFD. Used grid number is significant while solving pressure distribution and generated force. Although a larger mesh size for FDM gives high accuracy, computationally makes it slower. As Neural Network will be used, a mesh convergence study is performed, and a sufficient number of mesh is determined for the accuracy of pressure distributions.

Comparison of non-dimensional pressure distribution over the journal surfaces for viscous only (zeroth order) and inertial (first order) terms are given for a specific

case in which L/D is equal to 0.25 and eccentricity ratio is equal to 0.3. Reynolds number is equal to 5 is taken. The particular case is chosen because it occurs in the numerical case study, one of the cases in [35]. The pressure fields are shown in Figure 4.12 - Figure 4.14.

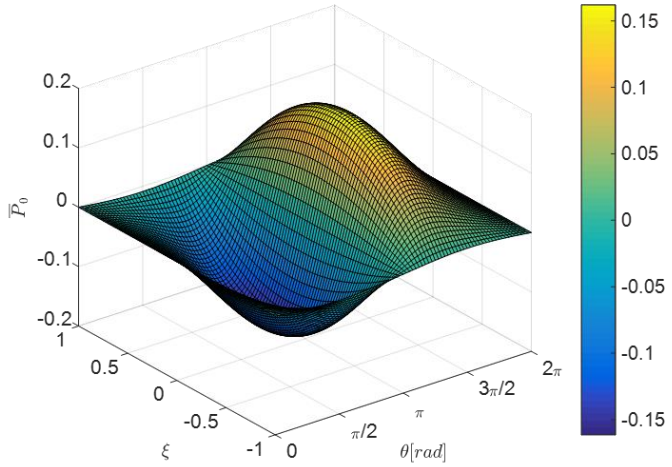

Figure 4.12: Viscous only pressure field

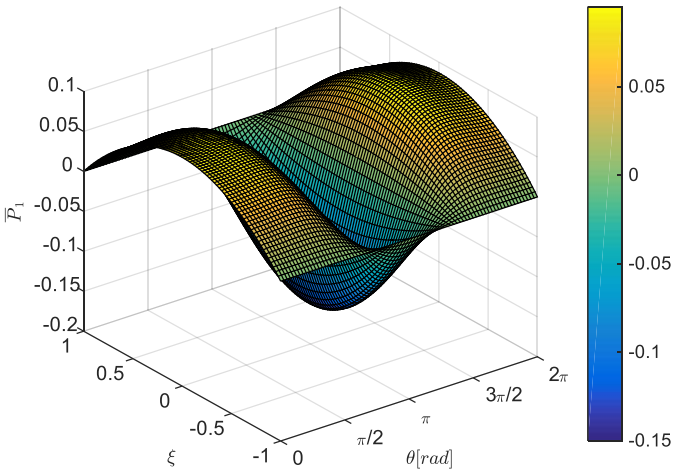

Figure 4.13: Inertial pressure field

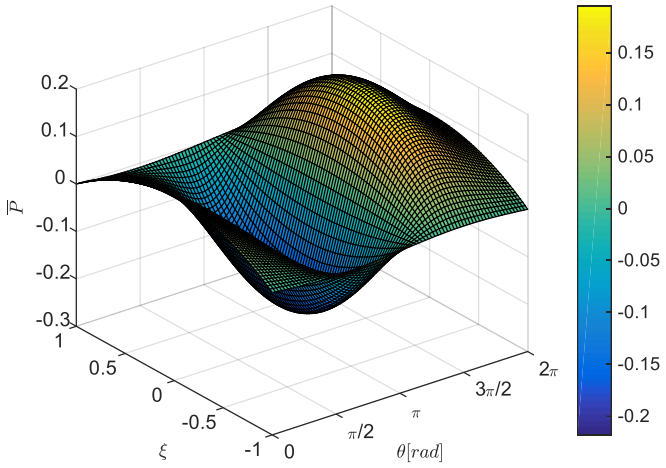

Figure 4.14: Total pressure field

Although Pressure fields show that viscous only pressure field is dominant with respect to the inertial pressure field, the inertial pressure field is considerable. Especially for larger Reynolds number, the inertial pressure field is significant. On the other hand, the distribution of pressure fields over the circumferential direction shows a different behavior between viscous only and inertial pressure fields. Their peak locations are at different circumferential coordinates, which may considerably affect the summation of pressure fields.

Viscous only and total pressure distributions with respect to the circumferential direction at the mid-plane of the SFD for different specific cases are studied. In specific cases, different Reynolds numbers are investigated. Firstly, *L/D=0.25* and *ε=0.1* case pressure distribution at SFD mid-plane is given in Figure 4.15.

Reynolds Number changes effects the pressure distribution in the aspect of the amplitude of pressure and location of the peak pressure at a circumferential coordinate. Secondly, *L/D=0.25* and *ε=0.3* case pressure distribution at SFD mid-plane is given in Figure 4.16. Lastly, *L/D=0.25* and *ε=0.5* case pressure distribution at SFD mid-plane is shown in Figure 4.17.

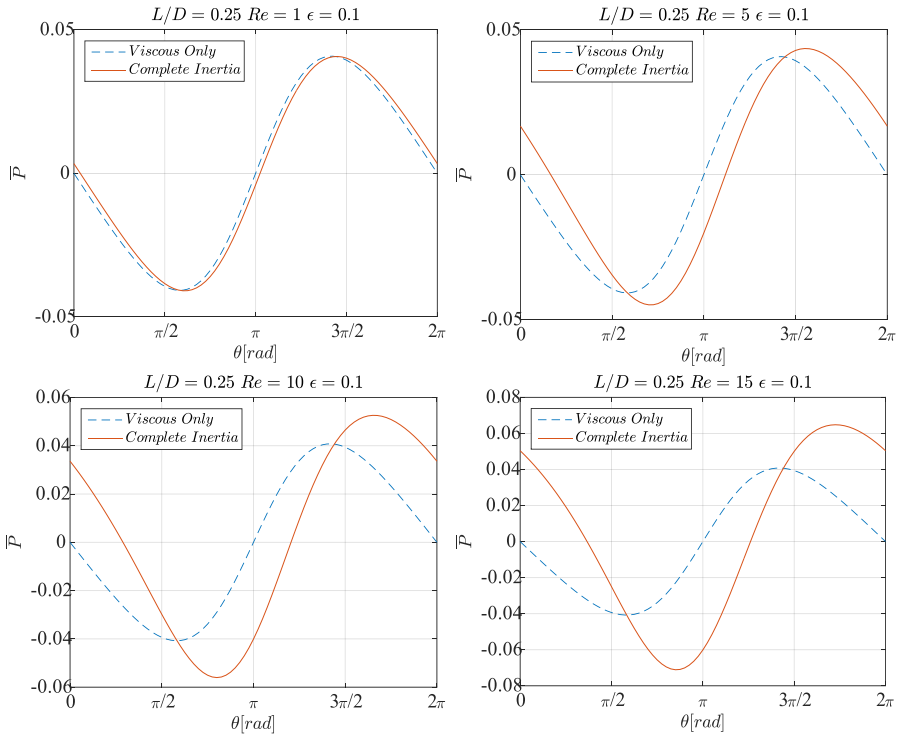

Figure 4.15: Pressure field at SFD mid-plane for *L/D=0.25* and *ε=0.1*

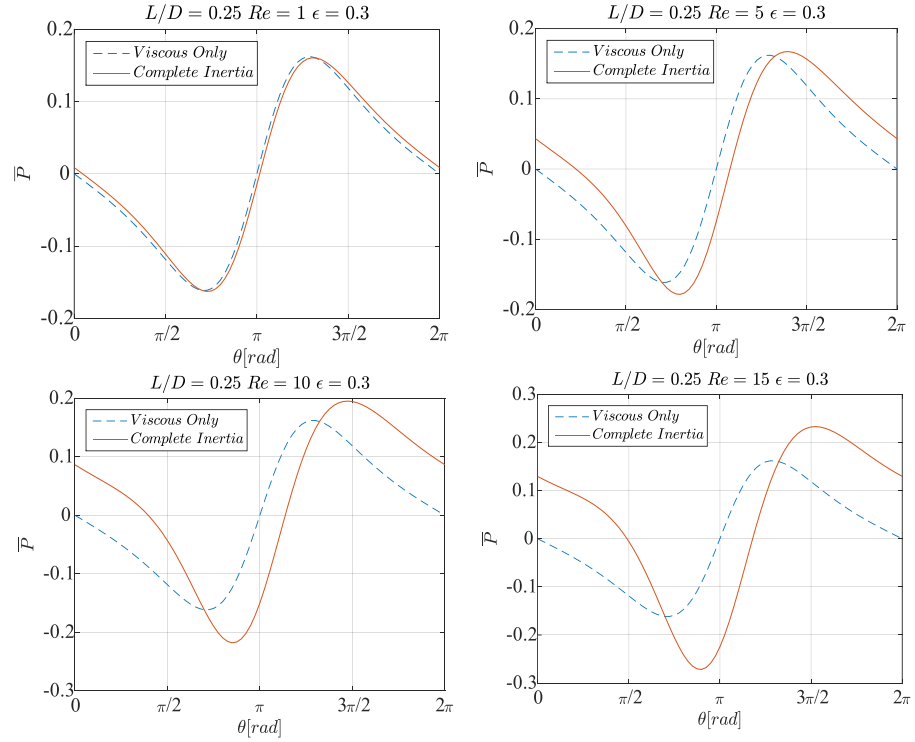

Figure 4.16: Pressure field at SFD mid-plane for *L/D=0.25* and *ε=0.3*

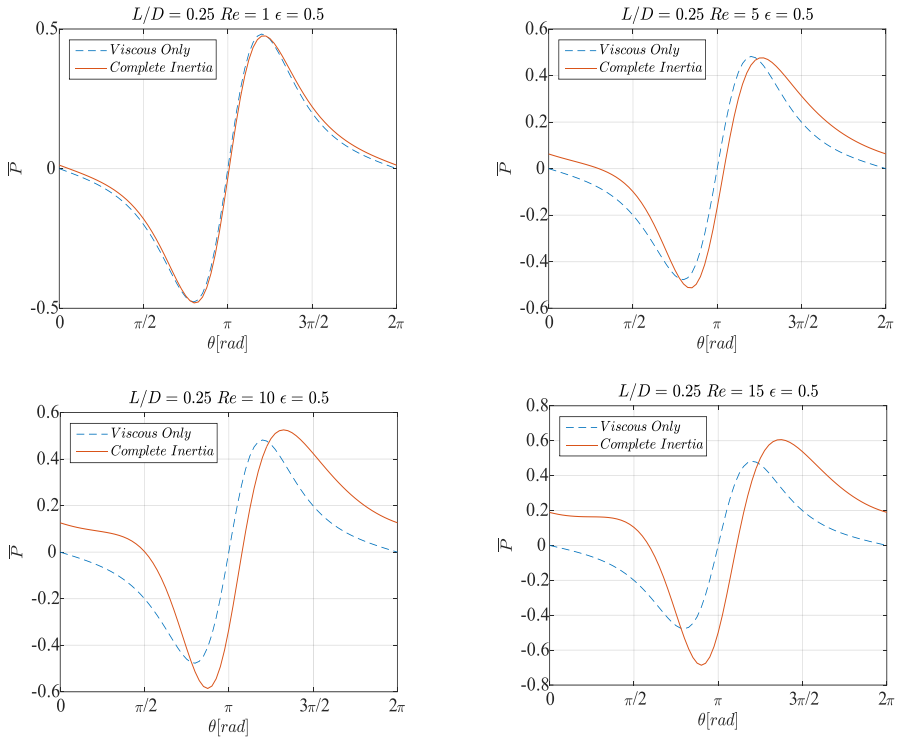

Figure 4.17: Pressure field at SFD mid-plane for *L/D=0.25* and *ε=0.5*

It is observed from Figure 4.15 - Figure 4.17 pressure field is drastically affected by the eccentricity ratio. Pressure magnitude is increasing with the increase of eccentricity ratio, and also, generated force is increasing. Furthermore, phase shifting occurs with the increase of eccentricity ratio. Reynolds number increase is increasing pressure magnitude and shifting peak locations of pressure distribution. The pressure field for a small Reynolds number is approximately the same with viscous only pressure distribution. However, moderate and high Reynolds numbers significantly affect pressure distribution, which should be considered. Moreover, these figures show good agreement with the literature [35].

The effect of the change of L/D ratio on pressure distribution is investigated for a specific case and given in Figure 4.18. The pressure magnitude increases with the increase of the *L/D* ratio. The relationship between *L/D* and pressure magnitude is not as linear as between eccentricity ratio and pressure magnitude.

Non-dimensional generated radial and tangential forces are given in Figure 4.19 and Figure 4.20 for different eccentricity ratios and Reynolds numbers at specific *L/D=0.25.*

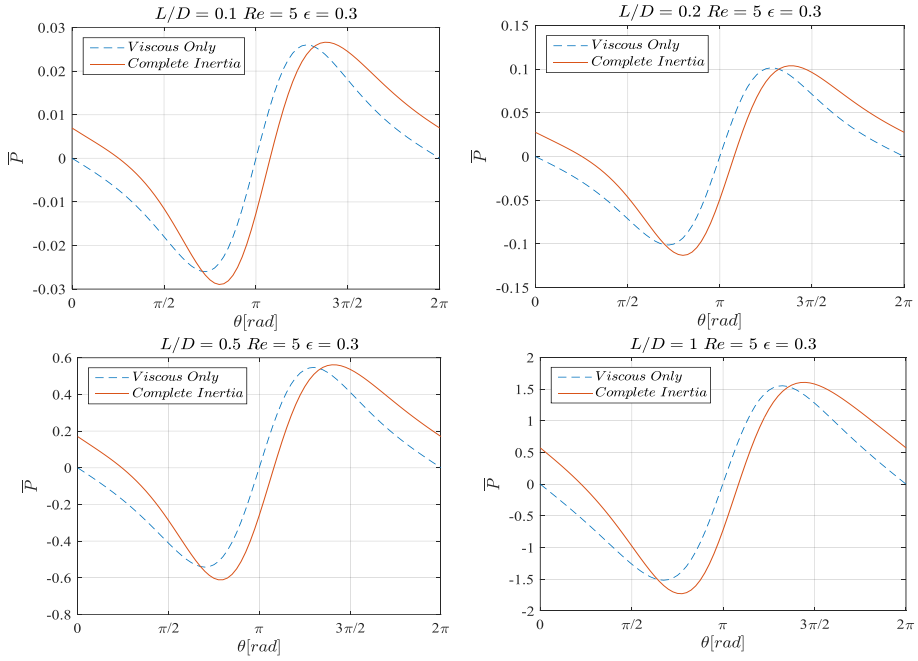

Figure 4.18: Pressure field at SFD mid-plane for *Re=5* and *ε=0.3*

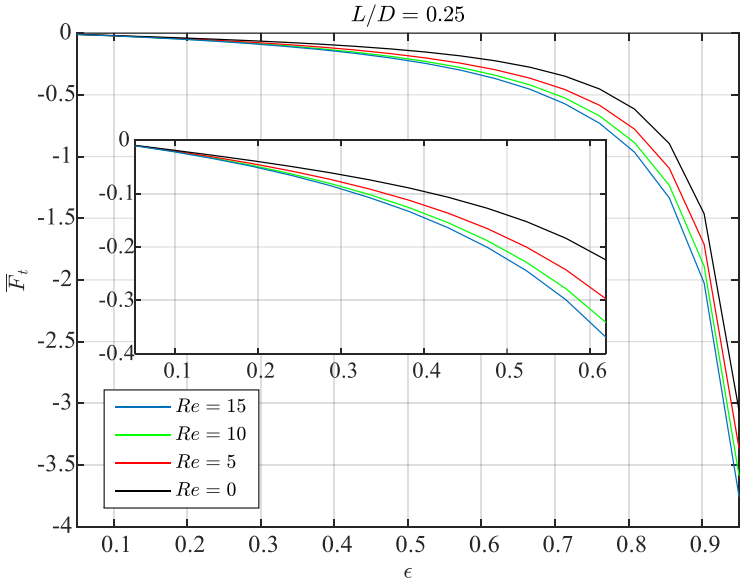

Figure 4.19: Non-Dimensional tangential force

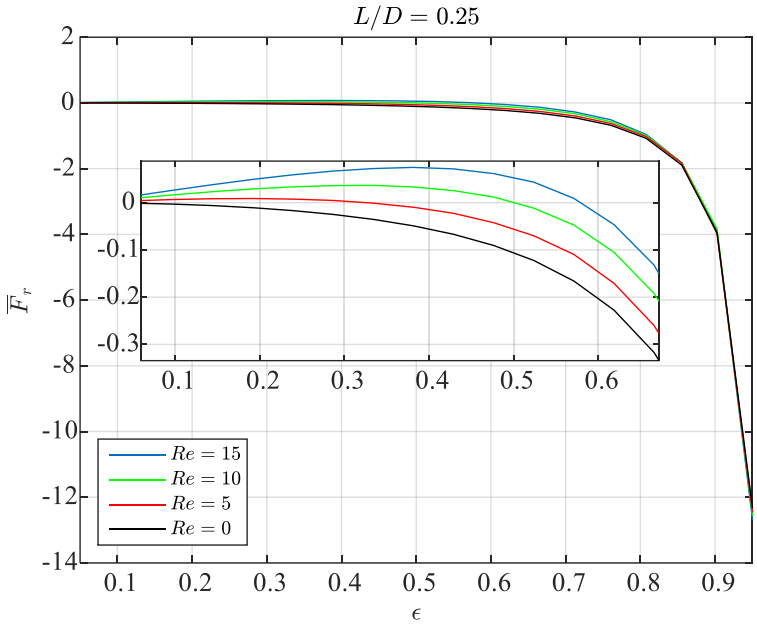

Figure 4.20: Non-Dimensional radial force

It is observed from Figure 4.19 and Figure 4.20 non-dimensional tangential force magnitude is increasing with eccentricity ratio in the negative direction for all Reynolds numbers. A Higher Reynolds number gives a higher magnitude for tangential force in the negative direction. In radial force, magnitude increases with eccentricity ratio increase in the negative direction for fluid inertia effect excluded case (*Re=0*). When the Reynolds number is larger than zero, radial force gives positive results for a small eccentricity ratio depending on the Reynolds number. When a higher Reynolds number is applied, i.e., Re =15, it hits a peak around 0.4 eccentricity ratio and turns negative values around 0.55 eccentricity ratio. It still gets a higher magnitude in the negative direction while the eccentricity ratio increases. While Reynolds number decreases, the positive portion of radial force with respect to eccentricity ratio decreases. Non-dimensional forces show slower changes and nearly linear behavior, up to ε = 0.4, which is also stated in [37]. However, these forces change drastically when the eccentricity ratio gets more significant. Furthermore, as expressed in Eq. (2-56), the radial force is related to stiffness, and tangential force is associated with viscous damping in the structural system by assuming the CCO motion type. Therefore, it can be concluded that the damping

capacity and stiffening effect increase while the eccentricity ratio increases, and the damping capacity increases while the Reynolds number increases. Reynolds number positively contributes to radial force, reducing stiffening effect and bi-stable rotor operation.

Non-dimensional generated radial and tangential forces are given in Figure 4.21 for different length-to-diameter ratios (*L/D*) and Reynolds numbers at specific ε = 0.3.

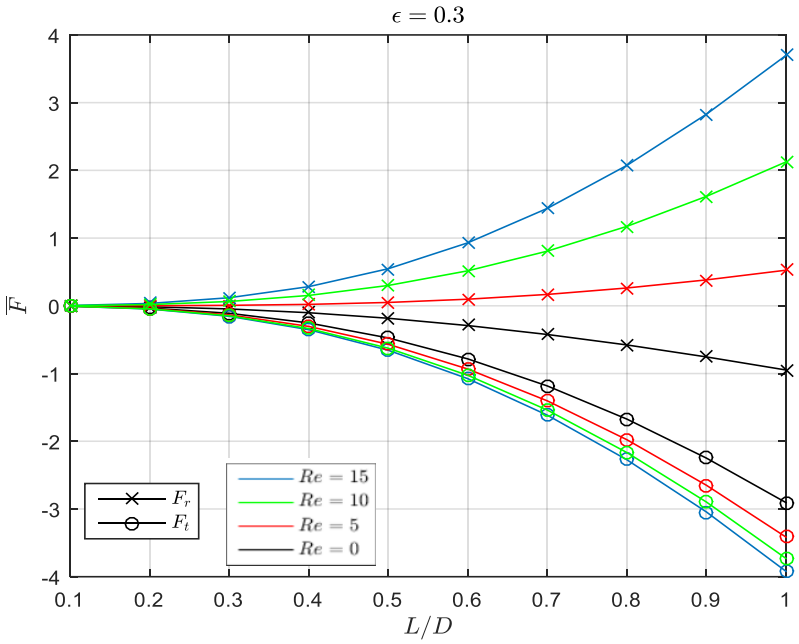

Figure 4.21: Non-dimensional Tangential and Radial Force with respect to Length to Diameter Ratio

It is seen that tangential force magnitude increases with length to diameter ratio increase and radial force increases except for *Re=0* case with length to diameter ratio increase. For *Re=0* case, radial force magnitude increases in the negative direction. It can be concluded that increasing the *L/D* ratio increases damping capacity, and a higher Reynolds number gives higher damping capacity. A Higher *L/D* ratio gives a higher stiffening effect. Note that these changes affect how much damping capacity and stiffening effect is case dependent and can be clearly seen from the nonlinear vibration frequency response, which will be given in the following section. As it is

only for ε = 0.3 case, it can be assessed with Figure 4.19 and Figure 4.20 for different eccentricity ratio cases.

4.3.2 Neural Network Study for SFD

A Neural Network study is performed to obtain nonlinear generated non-dimensional radial and tangential forces due to SFD with 27000 data sets. Input and output parameters are given in Table 2.2. The selection of input data is a vital process to represent outputs accurately. Therefore, an input data sensitivity study is performed by generating plenty of figures like Figure 4.19, Figure 4.20, and Figure 4.21. It can be summarized that data increment is smaller for eccentricity ratio is higher than 0.4 because the outputs, i.e., radial and tangential forces, change drastically. A similar approach is applied to *L/D* ratio. Outputs changes more for *L/D* ratio is higher than 0.3. It is observed that output changes show nearly linear behavior with the changes in Reynolds number. Therefore, Reynolds number increment is taken as linear in the range.

After defining the adequate number of the input set, non-dimensional radial and tangential forces are solved for these input sets by using the FDM described before. Obtaining the output data set takes around a 1-day run time.

Two different networks are studied and described in Table 2.2. They are compared in the aspect of nonlinear vibration response. The nonlinear vibration responses of FDM, network with two hidden layers, and network with three hidden layers are given in Figure 4.22, and Figure 4.23 for the case that *0.36 g-mm* and *0.79 g-mm* unbalance is applied at disk 1 (node 4) and nonlinear response is at the same location disk 1 (node 4).

It is observed that the three hidden layer network agrees well with the FDM result for both cases. The maximum difference in amplitude between 3 hidden layer network and FDM is %0.05 for *0.36 g-mm* case and %0.1 for *0.79 g-mm* cases. 2 hidden layer network shows close results with FDM except for peak locations. In the peak locations, 2 hidden layer network gives different amplitude with a slight

difference and different peak frequency. The maximum difference in amplitude between 2 hidden layer network and FDM is %2 for *0.36 g-mm* case and %0.8 for *0.79 g-mm* cases. Furthermore, the maximum difference in peak amplitude frequency between 2 hidden layer network and FDM is %3 for *0.79 g-mm* case. 3 hidden layer networks show very close results for all frequency regions for the given cases. Although the training computational time required for 3 hidden layers network is three times larger than 2 hidden layer network, training time is not very high given in Table 2.3, and considerable accuracy improvement is observed in a network with 3 hidden layers. Therefore, the network with 3 hidden layers is chosen for further comparisons and responses.

The computational time for obtaining nonlinear vibration responses is shown in Figure 4.22 and Figure 4.23 for FDM and Neural Network (NN) solutions in Table 4.4.

Table 4.4: Computational time comparison of FDM and NNs

Cases	**Method**	**Computational time (s)**
0.36 g-mm	FDM	5278 (%100)
	NN with 2 hidden layers	56 (%1.05)
	NN with 3 hidden layers	74(%1.4)
0.79 g-mm	FDM	8624 (%100)
	NN with 2 hidden layers	84 (%0.9)
	NN with 3 hidden layers	101(%1.1)

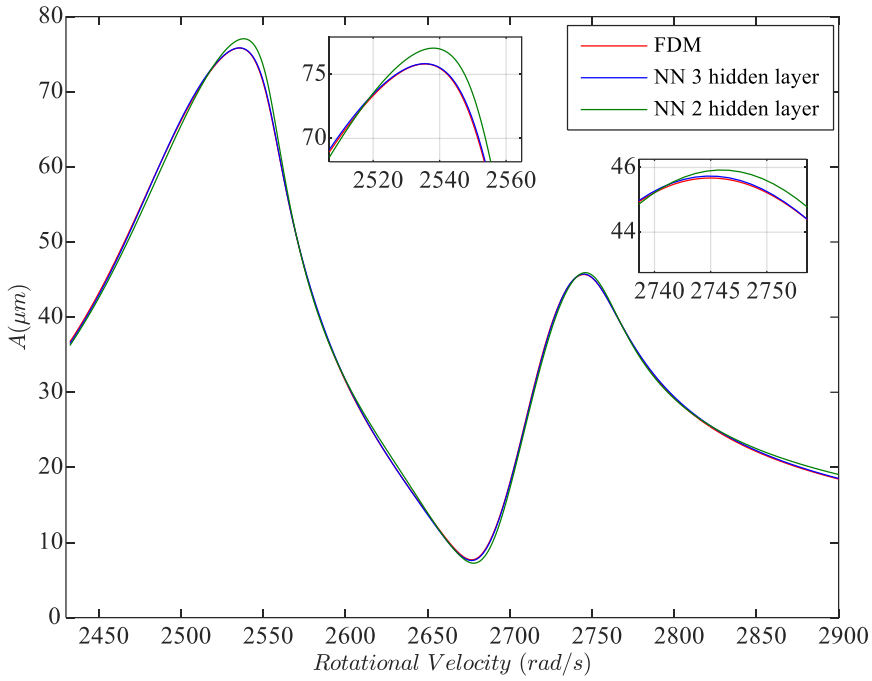

Figure 4.22: Nonlinear vibration responses of FDM and NNs 0.36 g-mm unbalance excitation at disk 1

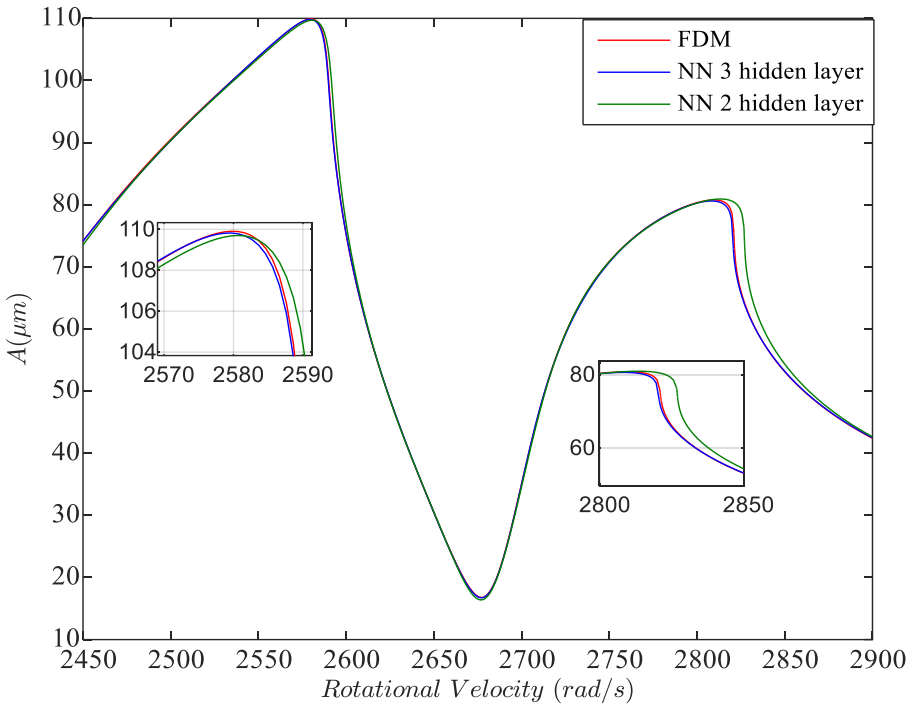

Figure 4.23: Nonlinear vibration responses of FDM and NNs for 0.79 g-mm unbalance excitation at disk 1

Usage of Neural Network significantly reduces computational time with respect to FDM. Although the analytical solution of SFD is applicable *L/D* ratio is smaller than 0.25, the FDM solution of pressure distribution is still significantly beneficial for the inclusion of fluid inertia effect and a more accurate solution. Regarding computational time, FDM requires much more time, so network usage has huge advantages in computational time with respect to FDM solution and gives good accuracy. A comparison of a network with 2 hidden layers and 3 hidden layers shows no significant shift in computational time, so a more accurate network with 3 hidden layers network can be used for further studies.

4.3.3 Nonlinear Vibration Responses Comparison between FDM and Neural Network

Non-dimensional input parameters for Neural Network (ε, *L/D,* and *Re*) effects are investigated on nonlinear vibration responses for the rotor dynamic system described in the previous sections.

0.5 gr-mm unbalance is applied at disk 1, and nonlinear responses at disk 1 are shown in Figure 4.24 for different *L/D* ratios. In the base case, *L/D* ratio is equal to 0.25.

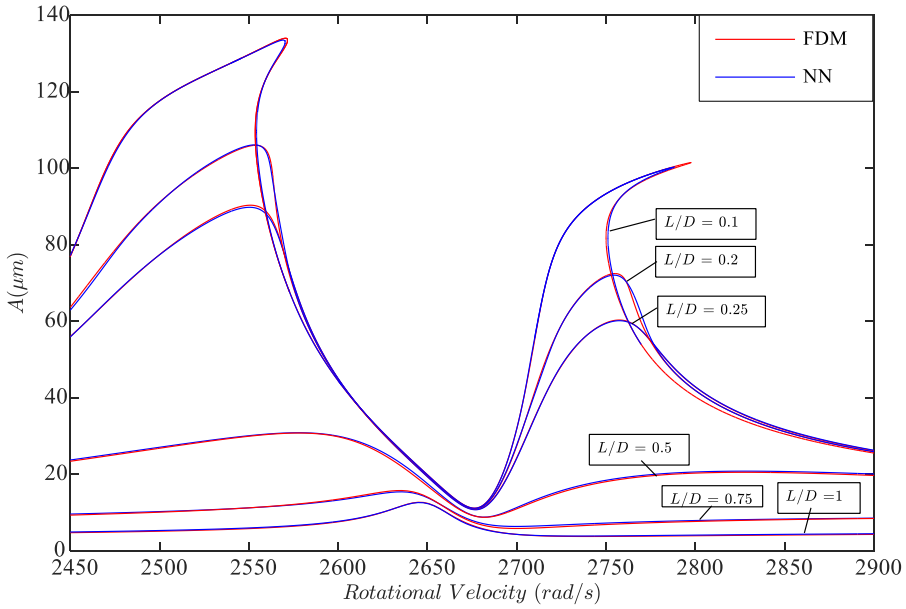

Figure 4.24: Nonlinear vibration responses at disk 1 for different L/D ratio

Nonlinear vibration responses are obtained for *L/D = 0.1, 0.2, 0.25, 0.5, 0.75* and *1*. As *L/D* ratio decreases from 0.25 to 0.1, damping capacity decreases, and the stiffening effect is observed. The jump phenomenon is seen for *L/D = 0.1* case and the amplitude of vibration increases. As *L/D* ratio increases from 0.25 to 1, damping capacity increases more, and amplitudes get smaller. The peak response frequency is shifting right with the increase of *L/D* ratio from 0.25 to 1. These are expected from the investigation of radial and tangential force changes with respect to *L/D* ratio. Furthermore, Neural Network (NN) shows close agreement with FDM for all *L/D* ratios. For *L/D = 0.1* case, NN and FDM show a small difference in peak amplitude and peak amplitude frequency for the 2nd mode. As the good agreement is observed for all frequency sweeps except peak locations, it is most probably caused that NN simulation shows differences for high eccentricity ratio, which is highly nonlinear region in the aspect of generated radial and tangential forces.

0.79 gr-mm unbalance is applied at disk 1, and nonlinear responses at disk 1 are shown in Figure 4.25 for different Reynolds numbers. Note that base case *Re* is around 5 for the range of frequency interest. Nonlinear vibration responses are obtained for *Re=0,5,10* and *15*. First of all, it is observed that the fluid inertia effect is important, especially for high Reynolds number values in nonlinear responses. As Reynolds number increases, damping capacity increases, and vibration amplitude is reduced. While Reynolds number decreases, damping capacity is reduced, which yields higher amplitudes and higher radial force is generated, then a stiffening effect occurs. The peak amplitude frequency shifts towards the right when the Reynolds number decreases. Furthermore, it is observed that NN simulation gives good agreement with FDM for different Reynolds numbers.

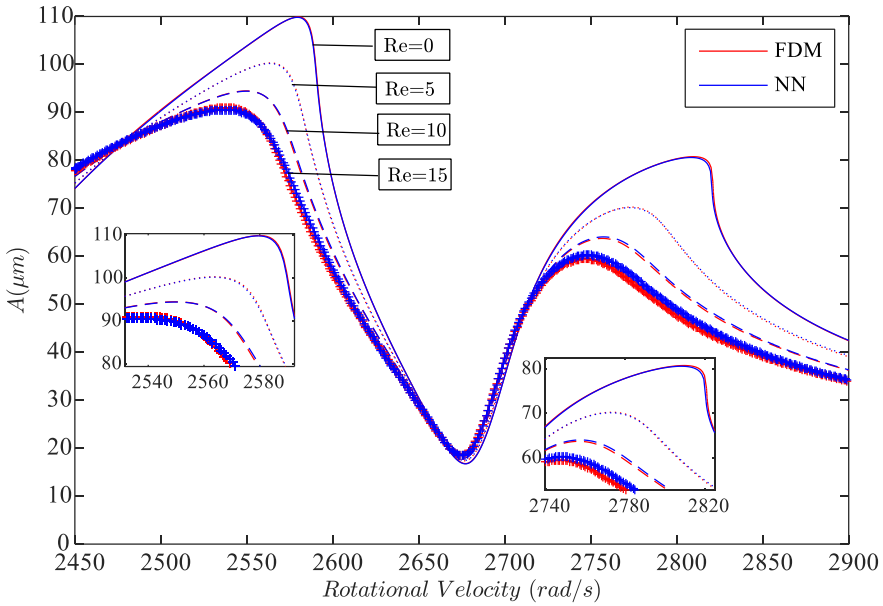

Figure 4.25: Nonlinear vibration responses at disk 1 for different Reynolds Number

4.3.4 Nonlinear Vibration Responses for effects of operation parameters

The amount of unbalance loading and viscosity can be changed in the operation of the rotor-bearing system. The amount of unbalance is affected by wear and the event of a compressor or turbine blade break. Viscosity is changed with the change of temperature of working fluid in SFD. Therefore, their changes should be taken into account in design processes. The amount of unbalance loading and viscosity of SFD oil effects on nonlinear vibration response are investigated using a Neural Network simulation model for SFD.

Normalized nonlinear vibration responses at disk 1 are shown in Figure 4.26 for a different amount of unbalance applied at disk 1. Note that the base case unbalance amount is *0.36 gr-mm*.

Nonlinear vibration responses are obtained for *U = 0.18 gr-mm, 0.36 gr-mm, 0.54 gr-mm, 0.72 gr-mm, 0.9 gr-mm* and without SFD case i.e., normalized linear vibration response. First of all, SFD gives a high amount of attenuation to vibration responses. Although absolute vibration amplitude increases for a higher amount of unbalance, normalized nonlinear responses decrease, which is caused by the that

higher unbalance generates a high eccentricity ratio and gives more damping capability. Furthermore, peak amplitude frequency shifts towards the right for both modes as the amount of unbalance gets higher. At %250 unbalance case, nonlinear vibration response shows high nonlinearity and jump phenomenon probability for 2nd mode. As a higher eccentricity ratio occurs for a higher amount of unbalance, generated radial force increases, and the stiffening effect increases.

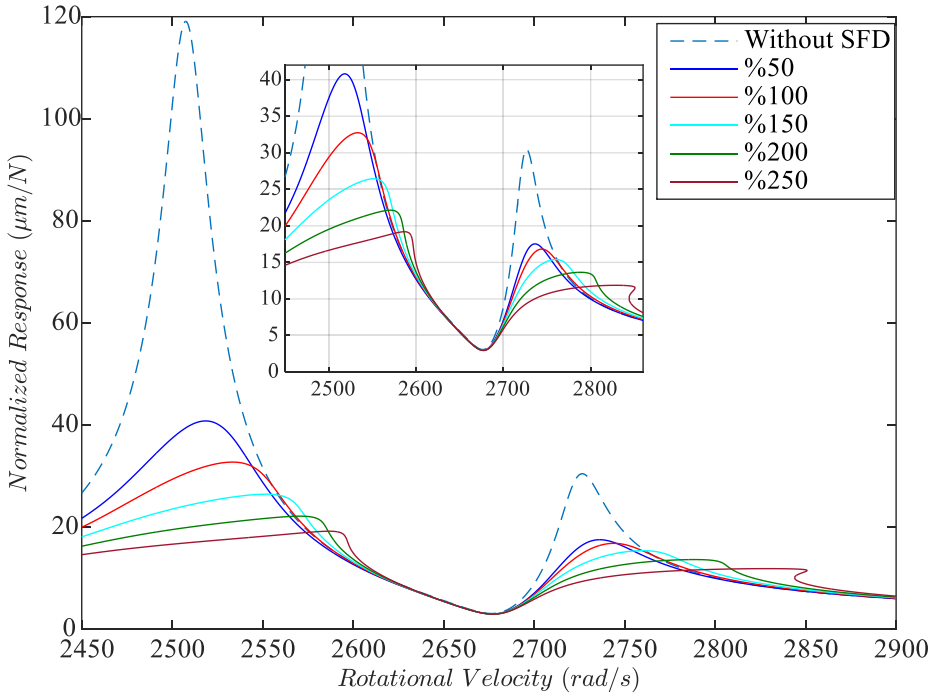

Figure 4.26: Normalized Nonlinear vibration responses for a different amount of unbalance loadings

0.79 gr-mm unbalance is applied at disk 1, and nonlinear vibration responses at disk 1 are shown in Figure 4.27 for different viscosity values. Oil viscosity can be changed during operation due to increased temperature. For example, a 20 K increase in oil temperature leads to a three times lower viscosity, and an 80 K increase in oil temperature leads to a ten times lower viscosity [40]. Therefore, change of viscosity value should be investigated for nonlinear vibration response. Note that the base case viscosity value is *5 centipoise.* Nonlinear vibration responses are obtained for μ = *1.25, 2.5, 5, 7.5* and *15 centipoise.* Higher viscosity values give higher attenuation on nonlinear vibration responses as expected; however, it may not be available for

higher operating temperatures. As viscosity increases from 2.5 centipoise to 15 centipoise, nonlinear vibration responses decrease, peak amplitude frequency shifts towards the right, and the stiffening effect is observed. Vibration amplitude increases as viscosity decreases from 2.5 to 1.25 centipoise, and peak amplitude frequency shifts towards the right, which is a stiffening effect. Nonlinearity becomes larger for lower viscosity values, especially when viscosity equals 1.25 centipoise. The jump phenomenon probably gets higher for 1st and 2nd modes.

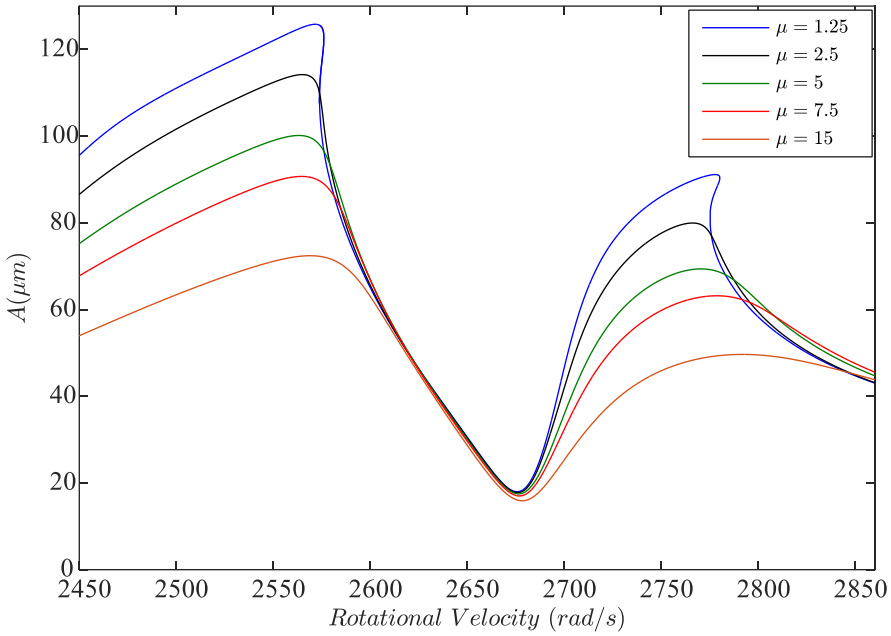

Figure 4.27: Nonlinear Vibration responses for different viscosity values

CHAPTER 5

CONCLUSION

In this thesis, nonlinear vibration of rotor-bearing system supported by Squeeze Film Damper (SFD) is presented. The Linear Rotor-bearing system model is developed by 1-D Timoshenko beam elements.

Firstly, the solution of the 1D Reynolds equation of SFD is utilized to model SFD. The theoretical background of the rotordynamic model, nonlinear short-length squeeze film damper model, and solution procedure is presented. A small turbojet engine available in the literature [27] is considered as a case study. A single SFD is connected to the system close to the first lumped masses. Effects of cavitation type in SFD lubricant, fluid inertia contribution, geometrical dimensions such as diameter, length, and clearance of the SFD, the amount of unbalance, and its location on the nonlinear response are presented. Results show that the nonlinear forced response of the rotor-bearing system highly depends on the parameters of the SFD, especially the clearance and the length of the SFD, and the journal's dynamic motion, which directly depends on the amount of unbalance and its location.

Secondly, the SFD model is developed with a 3D Reynolds equation solution using FDM, including oil inertia effects. Oil pressure distribution for viscous only (zeroth order) and inertial (first order) terms are solved by means of FDM for open-ended SFD by assuming CCO motion type. The nonlinear forces generated by SFD is obtained by integrating oil film pressure distribution over the journal surface. A Neural Network study is performed to model SFD to get a fast and accurate simulation model for SFD. Three non-dimensional inputs (ε, L/D, and Re) are necessary and sufficient in order to get non-dimensional radial and tangential forces outputs generated by SFD. A neural network simulation model is established and compared with the FDM solution of SFD nonlinear forces. Dynamic forces acting on SFD cause nonlinear forcing exerted on the rotor-bearing system. Therefore, the

rotor-bearing system and SFD coupling model is established. Nonlinear forces, including differential equations, are converted into a set of algebraic equations with HBM, and nonlinear equations are solved by Newton's method with arc-length continuation.

A numerical case study is performed. Oil pressure distribution and generated forces are presented for input parameters (ε, *L/D* and *Re*) of the Neural Network. 2 different networks are studied and compared. A network 3 hidden layer gives better accuracy while slightly increasing computational time. Nonlinear vibration responses are compared for the FDM solution of SFD and the Neural Network solution of SFD. The followings are observed that

- Neural Network (NN) solution agrees with the FDM solution SFD in nonlinear vibration responses for the cases of base SFD configurations. Furthermore, NN is computationally much more efficient than FDM, which NN solution requires around %1 time of FDM solutions for studied nonlinear vibration responses.
- For low *L/D* ratio and high eccentricity ratio, NN results have a slight difference with the FDM solution. It can be caused that those nonlinear generated forces may be changed drastically at higher eccentricity ratio regions. As *L/D* ratio increases, nonlinear vibration response decreases.
- For different Reynolds numbers, the NN solution gives close agreement with FDM. Nonlinear vibration responses decrease with the increase of Reynolds number because an increase of Reynolds number increases tangential force and damping capacity. Furthermore, it is seen that the Reynolds number is getting higher, and the effect of fluid inertia is getting significantly considerable for nonlinear vibration responses.
- Some parameters that can easily change the operating system, such as the amount of unbalance loading and viscosity effects, are investigated on nonlinear vibration responses. It is seen that the normalized response decreases, and nonlinearity becomes higher with the increase in the amount of unbalance loadings. While having higher viscosity increases the damping capacity, it shifts

the peak amplitude frequency towards right and for low viscosity values, nonlinearity becomes more significant, and amplitude increases.

The proposed methods provide fast and accurate modeling and nonlinear vibration response simulation. Especially for the design and analysis process for the rotor-bearing system supported by SFD, the Neural network solution of SFD has huge advantages in computational time and gives good accuracy.

REFERENCES

1. J. Vance, Rotordynamics of Turbomachinery, (1988), John Wiley and Sons, New York.

2. Childs, D.W. (1993) Turbomachinery Rotordynamics: Phenomena, Modeling, and Analysis. John Wiley & Sons Inc., New York.

3. Gunter, E. J., Barrett, L. E., and Allaire, P. E. (1975), “Design and Application of Squeeze Film Dampers for Turbomachinery Stabilization”, Proceedings of the Fourth Turbomachinery Symposium, Turbomachinery Laboratory, Texas A&M University, College Station, Texas, pp. 127–141.

4. Gunter, E. J., Barrett, L. E., and Allaire, P. E. (1977), "Design of Non-Linear Squeeze-Film Dampers for Aircraft Engines", ASME Journal of Lubrication Technology, 99, pp. 57–64.

5. San Andrés, L., 2012, "Squeeze Film Damper: Operation, Models and Technical Issues," Modern Lubrication Theory, Notes 13, Texas A&M University Digital Libraries, http://repository.tamu.edu/handle/1969.1/93197 [02/05/2013].

6. Cooper, S., "Preliminary Investigation of Oil Films for the Control of Vibration," Paper 28, Lubrication and Wear Convention, Instn Mech Engrs (1963).

7. White, D. C., "The Dynamics of a Rigid Rotor Supported on s·queeze Film Bearings," Proceedings of the Conference on Vibrations in Rotating Systems, London, pp. 2 1 3-229 (1972).

8. Zeidan, F., L. San Andrés, and J. Vance, "Design and Application of Squeeze Film Dampers in Rotating Machinery," Proceedings of the 25th Turbomachinery Symposium, Turbomachinery Laboratory, Texas A&M University, September, pp. 169-188, 1996.

9. Arauz, G. and San Andres, L., "Experimental Study on the Effect of a Circumferential Feeding Groove on the Dynamic Response of a Sealed Squeeze Film Damper," ASME Paper 95- Trib-50 (1995)

10. Arauz, G. and San Andres, L., "Effect of a Circumferential Feeding Groove on the Force Response of a Short Squeeze Film Damper," ASME Journal of Tribology, 116 (2), pp. 369- 377 (1994)

11. San Andres, L. and Vance, J. M., "Effects of Fluid Inertia and Turbulence on the Force Coefficients for Squeeze Film · Dampers," ASME Journal of Engineering for Gas Turbines and Power, 1 08, pp. 332-339 (1986).

12. Zeidan, F.Y., Vance, J.M.: Cavitation regimes in squeeze film dampers and their effect on the pressure distribution. Tribol. Trans. 33(3), 447–453 (1990). https://doi.org/10.1080/10402009008981975

13. Luis A. San Andres and J. M. Vance. Force coeffcients for open-ended squeeze film
dampers executing small-amplitude motions about an off-center equilibrium position. ASLE - Transactions, 30(1):69, 1987.

14. L. San Andrés, Theoretical and Experimental Comparisons for Damping Coefficients of a Short Length Open-End Squeeze Film Damper, ASME Journal of Engineering for Gas Turbines and Power, (1996), 118, pp. 810-815

15. TaylorDL and KumarBRK.Nonlinear response of short squeeze film dampers. J Lubr Technol 1980; 102: 51.

16. Taylor DL and Kumar BRK. Closed-form, steady-state solution for the unbalance response of a rigid rotor in squeeze film damper. J Eng Power 1983; 105: 551.

17. Mohan S and Hahn EJ. Design of squeeze film damper supports for rigid rotors. J Eng Ind 1974; 96: 976.

18. Hahn EJ. Stability and unbalance response of centrally preloaded rotors mounted in journal and squeeze film bearings. J Lubr Technol 1979; 101: 120.

19. R.A Cookson and S.S Kossa. The efectiveness of squeeze film damper bearings supporting rigid rotors without a centralising spring. International Journal of Mechanical Sciences, 21(11):639{650, 1979.

20. Rabinowitz MD and Hahn EJ. Stability of squeeze film damper supported flexible rotors. J Eng Power 1977; 99: 545.

21. Rabinowitz MD and Hahn EJ. Steady-state performance of squeeze film damper supported flexible rotors. J Eng Power 1977; 99: 552.

22. Zhao, J.Y., Linnett, I.W., Mclean, L.J.: Stability and bifurcation of unbalanced response of a squeeze film damped flexible rotor. J. Tribol. 116(2), 361–368 (1994). https://doi.org/10.1115/1.2927236

23. Zhao, J.Y., Linnett, I.W., Mclean, L.J.: Subharmonic and quasi-periodic motions of an eccentric squeeze film dampermounted rigid rotor. J. Vib. Acoust. Trans. ASME 116(3), 357–363 (1994). https://doi.org/10.1115/1.2930436

24. Inayat-Hussain JI. Bifurcations of a flexible rotor response in squeeze-film dampers without centering springs. Chaos Solitons Fract 2005; 24: 583–596.

25. Inayat-Hussain JI. Bifurcations in the response of a flexible rotor in squeeze-film dampers with retainer springs. Chaos Solitons Fract 2009; 39: 519–532.

26. Nelson, H. D., 1980, "A Finite Rotating Shaft Element Using Timoshenko Beam Theory," ASME J. Mech. Des., 102, pp. 793–803.

27. Genta, G., Dynamics of Rotating Systems, Springer, New York, 2005.

28. L. M. Greenhill and H. D. Nelson. Iterative determination of squeeze film damper eccentricity for flexible rotor systems. Journal of mechanical design, 104:334, 1982.

29. Mclean, L. J., and Hahn, E. J., 1983, "Unbalance Behavior of Squeeze Film Damped Multi-Mass Flexible Rotor Bearing System," ASME J. Lubr. Technol., 105, pp. 22–28.

30. Bonello, P., Hai, P.M.: A receptance harmonic balance technique for the computation of the vibration of a whole aero-engine model with nonlinear bearings. J. Sound Vib. 324(1–2), 221–242 (2009). https://doi.org/10.1016/j.jsv.2009.01.039

31. Lund, J.W., Smalley, A.J., Tecza, J.A., Walton, J.F.: Squeeze-film damper technology: part 1 - prediction of finite length damper performance. In: ASME. Turbo Expo:Power for Land, Sea, and Air, Phoenix, Arizona, USA. International Gas Turbine Institute (1983). https://doi.org/10.1115/83-GT-247

32. Tecza, J.A., Giordano, J.C., Zorzi, E.S., Drake, S.K.: Squeeze-film damper technology: part 2 – experimental verification using a controlled-orbit test rig. In: ASME.Turbo Expo: Power for Land, Sea, and Air, Phoenix, Arizona, USA. International Gas Turbine Institute (1983).https://doi.org/10.1115/83-GT-248

33. San Andres, L.A., Vance, J.M.: Effect of fluid inertia on the performance of squeeze film damper supported rotors. J. Eng. Gas Turbines Power 110(1), 51–57 (1988). https://doi.org/10.1115/1.3240086

34. Hamzehlouia, S., Behdinan, K.: First order perturbation technique for squeeze film dampers executing small amplitude circular centered orbits with aero-engine application.In: ASME 2016 International Mechanical Engineering Congress and Exposition, Phoenix, Arizona.International Gas Turbine Institute (2016). https://doi.org/10.1115/IMECE2016-65784

35. Hamzehlouia, S., Behdinan, K.: A study of lubricant inertia effects for squeeze film dampers incorporated into highspeed turbomachinery. Lubricants 5(4), 43–74 (2017).https://doi.org/10.3390/lubricants5040043

36. Hamzehlouia, S., Behdinan, K.: Squeeze film dampers supporting high-speed rotors: fluid inertia effects. Proc. Inst. Mech. Eng. Part J J. Eng. Tribol. 234(1), 18–32 (2020).https://doi.org/10.1177/1350650119855792

37. San Andrés, Luis; Jeung, Sung-hwa; Den, Sean; Savela, Gregory (2016). Squeeze Film Dampers: An Experimental Appraisal of Their Dynamic Performance. Turbomachinery Laboratories, Texas A&M Engineering Experiment Station.

38. Feng He., Paul Allaire., and Timothy Dimond., 2014. "Use of Harmonic balance method for flexible aircraft engine rotors with nonlinear squeeze film dampers". In Proceedings of the IDETC/CIE 2014 ASME conference, August 17-20, 2014, Buffalo, New York, USA.

39. Chen, X., Gan, X. & Ren, G. Nonlinear responses and bifurcations of a rotor-bearing system supported by squeeze-film damper with retainer spring subjected to base excitations. Nonlinear Dyn 102, 2143–2177 (2020). https://doi.org/10.1007/s11071-020-06052-0

40. Chen, X., Ren, G. & Gan, X. Dynamic behavior of a flexible rotor system with squeeze film damper considering oil-film inertia under base motions. Nonlinear Dyn 106, 3117–3145 (2021). https://doi.org/10.1007/s11071-021-06978-z

41. Von Groll, G., Ewins, D.J.: The harmonic balance method with arc-length continuation in rotor/stator contact problems. J. Sound Vib. 241, 223–233 (2001)

42. Menq, C.-H., Griffin, J. H., and Bielak, J., 1986, "The Forced Response of Shrouded Fan Stages," 108(January 1986), pp. 50–55.

43. Yavuz, S. D., Saribay, Z. B., and Cigeroglu, E., 2018, "Nonlinear TimeVarying Dynamic Analysis of a Spiral Bevel Geared System," Nonlinear Dyn., 92(4), pp. 1901–1919

44. Nelson, H. D., and McVaugh, J. M., 1976, "The Dynamics of Rotor-Bearing Systems Using Finite Elements," J. Eng. Ind., 98(2), p. 593.